Stimuli Responsive Barrier Materials for Breathable, Chemically-Protective Wearable

Fabrics

By

Kenneth Manning

A Dissertation Presented in Partial Fulfillment
of the Requirements for the Degree
Doctor of Philosophy

Approved June 2020 by the
Graduate Supervisory Committee:

Konrad Rykaczewski, Chair
Timothy Burgin
Heather Emady
Matthew Green
Marylaura Thomas

ARIZONA STATE UNIVERSITY

August 2020

ABSTRACT

As experiencing hot months and thermal stresses is becoming more common, chemically protective fabrics must adapt and provide protections while reducing the heat stress to the body. These concerns affect first responders, warfighters, and workers regularly surrounded by hazardous chemical agents. While adapting traditional garments with cooling devices provides one route to mitigate this issue, these cooling methods add bulk, are time limited, and may not be applicable in locations without logistical support. Here I take inspiration from nature to guide the development of smart fabrics that have high breathability, but self-seal on exposure to target chemical(s), providing a better balance between cooling and protection.

Natural barrier materials were explored as a guide, focusing specifically on prickly pear cacti. These cacti have a natural waxy barrier that provides protection from dehydration and physically changes shape to modify surface wettability and water vapor transport. The results of this study provided a basis for a shape changing polymer to be used to respond directly to hazardous chemicals, swelling to contain the agent.

To create a stimuli responsive material, a novel superabsorbent polymer was synthesized, based on acrylamide chemistry. The polymer was tested for swelling properties in a wide range of organic liquids and found to highly swell in moderately polar organic liquids. To help predict swelling in untested liquids, the swelling of multiple test liquids were compared with their thermodynamic properties to observe trends. As the smart fabric needs to remain breathable to allow evaporative cooling, while retaining functionality when soaked with sweat, absorption of water, as well as that of an absorbing liquid in the presence of water were tested.

Micron sized particles of the developed polymer were deposited on a plastic mesh with pore size and open area similar to common clothing fabric to establish the proof of concept of using a breathable barrier to provide chemical protection. The polymer coated mesh showed minimal additional resistance to water vapor transport, relative to the mesh alone, but blocked more than 99% of a xylene aerosol from penetrating the barrier.

ACKNOWLEDGMENTS

TABLE OF CONTENTS

LIST OF FIGURES

CHAPTER 1

INTRODUCION AND BACKGROUND

1.1 General Background

Semi-permeable membranes are ubiquitous in both manmade and natural

materials. In nature, functionalized membranes range in complexity from those

surrounding single celled organisms and cell organelles, to highly sophisticated multi-

layer protection systems like skin. While natural barriers are very effective in blocking

many potential hazards, there is a clear need for additional protection from harmful

agents for people in all walks of life. The Covid-19 pandemic has exposed how effective,

accessible barrier materials are critical to protecting people and maintaining lifestyles.

Further, living in Phoenix has highlighted a significant limitation of protective materials

as the pandemic extends into the summer. Specifically, barrier materials such as face

masks reduce our bodies' ability to cool itself, increasing thermal stress and impacting

our ability to perform activities that require exertion.

The additional thermal loads associated with working in hazardous conditions are

driving innovation to increase heat transfer for personal protective garments[1] while

maintaining their protective qualities.[2–6] Throughout this thesis, I will focus on personal

protective equipment (PPE) but these needs extend beyond just personal protection. For

example, many nations still have the capability to release extremely toxic liquids with

low vapor pressure deliberately to inflict damage in target populations.[7] Rapid and

efficient capture of such toxins is important in preventing lingering hazards due to

absorption into surrounding porous materials including polymers, vehicle coatings, and

dust. A failure to do so poses a continuing toxicological threat, worsened by the fact that

these contamination zones are nearly impossible to fully contain.[8] These concerns are echoed in accidental spills where people and the environment are exposed to hazardous materials.

Because of the simultaneous dangers of heat stress and chemical exposure in PPE, research is being conducted to provide workers and warfighters with ways to alleviate both stressors. Two main avenues of research have been explored to aid these high risk workers: active cooling systems[9,10,19,11–18] and breathable systems[2–6] to augment natural cooling. Active cooling systems generally rely on external, battery powered heat exchangers to circulate a cooling medium (e.g. water) to keep the wearer cool. Other active cooling systems involve using phase change materials that provide a limited window of cooling.[20,21] The alternative to these systems is to provide a more breathable material that allows for natural evaporative cooling to take place.

Protection of US military personnel is currently mandated by mission oriented protective postures (MOPP), which outline addition protection to be worn over the standard military uniform as chemical and biological threat levels increase. As the MOPP gear, shown in Figure 1.1 is added, the overall breathability is reduced, with the most restrictive level (MOPP 4) being nearly impermeable, similar to a commercial hazmat suit. These guidelines were developed in an attempt to balance augmented protection with the resulting increased thermal load and impacts on performance. As a means of mitigating these tradeoffs, the military is currently looking to transition to protective garments made from breathable fabrics to provide warfighters protection from chemical warfare agents (CWAs).

Figure 1.1 Illustration of the MOPP levels highlighting the required additional garments warfighters need to carry and wear to protect against potentially hazardous conditions.[22]

MOPP garments are heavy and take time to don and doff. As a result of the heat stress limitations and decreased functionality, warfighters only wear the gear required for a given threat level. While at higher MOPP levels, even moderate exertion in a temperate climate, as seen in Figure 1.2, can cause hyperthermia in as little as 45 minutes.[10,23] The current guidelines for breathability are typically around the breathable fabric threshold of 2000 gm^{-2} per 24 hours,[24] which allows for an equivalent of about 100 W of evaporative cooling for a fully clothed average sized adult (~ 2 m^2 of clothing). This cooling rate only addresses metabolic heat generation of an idle individual that is not experiencing environmental heating.[25] Thus, many MOPP fabrics do not provide a sufficient degree of breathability to be worn for extended periods of time during operations in hazardous areas.
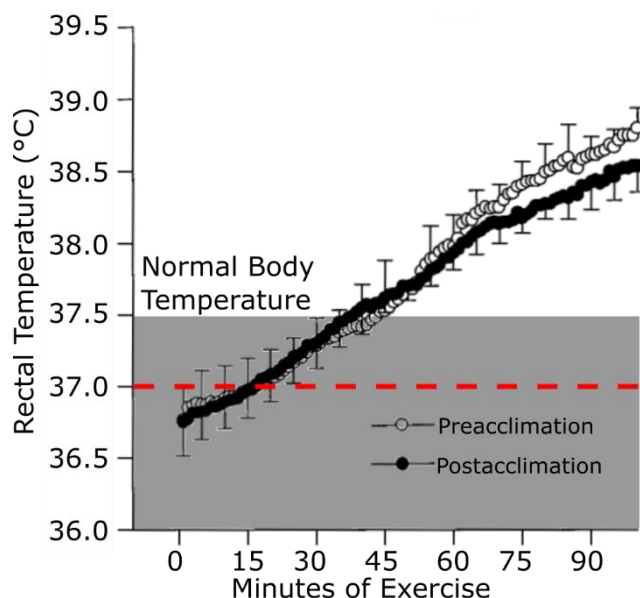
Figure 1.2 Heat strain in Air Force chemical protective clothing done by Gonzalez et al.[23] against minutes of moderate exercise in a 35°C environment. The gray area indicates normal body temperatures (red highlights expected mean body temperature) and highlights deviation into hyperthermia.

A variety of technologies are emerging to meet the need for providing MOPP gear with increased breathability that maintain a sufficient level of protection from chemical warfare agent threats. While CWA was banned by the Geneva Protocol in 1925,[26] and nearly all countries have signed the Chemical Weapons Convention[27], they remain a dangerous and current threat, still in use today. The gas attacks during the Syrian civil war and other conflicts[28–31] have highlighted the continued need for CWA protection, and capability gaps of the currently used technologies. In particular, conflicts in areas like Syria also highlight challenges in thermoregulation, due to the extremely high temperatures that occur in the region. A number of groups are exploring different options to overcome these challenges. Current approaches include several selective barrier membranes based on carbon nanotubes,[32,33] graphene oxide flakes,[4,5] and polymers with selective pores for vapor tansport[3,34,35] have shown promise in protecting against CWA

4

penetration while allowing some water vapor transport. These barrier materials tend to be expensive to produce,[36] provide minimal additional breathability,[3,4] and carry potential hazards of their own (e.g. carcinogenic).[37]

A protective fabric with integrated polymers that swell on contact with CWAs has the potential to provide cheap, highly breathable personnel protection. Broadly, swelling is an extremely common phenomenon in polymers but the ability for a polymer to swell highly in a specific liquid is rarer. There are a multitude of hydrogel materials that will absorb water and swell hundreds of times their original size.[38–40] These gels are used widely as sorbent materials,[41–45] diffusers,[46–48] and low modulus biological supports.[49–51] While hydrogels are relatively common, highly swelling oil sorptive polymers are relatively rare. Some examples have been created using electrolytic materials,[52,53] but the presence of reasonably polarizable liquids disrupts their swelling capabilities.

By using these high swelling capabilities, a fabric can remain mostly open and breathable prior to exposure. Once the polymer comes into contact with the target liquid(s), absorption closes off the pores, creating a layer of swollen gel that blocks the penetration of any additional chemical that contacts the swollen region. In addition, by swelling with the hazardous material, the polymer can contain the materials from migrating and potentially contacting a different area. This method of action provides the user with comfortable, breathable protection while also containing the hazard and thus stopping any further spread. When combined with a heterogeneous decontaminant these materials could potentially provide a complete personal protection solution. These polymeric sorbent materials can also be used on spills that need to be cleaned up

5

effectively. By adding a high swelling polymer, the gelled material can be more easily disposed of without concern of a flowing liquid.

1.2 Structure of Thesis

The objective of this thesis is to provide a fundamental look at how the development of new polymeric materials can be used in response to chemical threats. Eventually, I explore how these materials can be used as a stimuli-responsive barrier material and their potential applications as a breathable, chemically protective fabric. In Chapter 2, I will introduce some biological inspiration relating to the development of swelling and sealing materials. This chapter explores how the mechanical swelling and deswelling of prickly pear cacti can assist in the regulation of cactus hydration. This work provided some insight into how much swelling can affect mass transfer rates through barrier materials and helped guide some of my work in developing composite materials.

In Chapter 3, I discuss the development of the super absorbent polymeric material I developed for this application. I explore the swelling capabilities of the polymer and highlight the effects of minor changes to the polymer structure dramatically changing the swelling capabilities. This work provides both the materials to be used in developing the barrier material as well as some insights into how swelling can be related to solvent-polymer properties, specifically to be able to predict swelling with simple swelling experiments. This work provided a springboard to then begin exploring the use of these materials for composite fabric membranes.

Chapter 4 develops the work from Chapter 3 further, exploring breathability of fabrics and combining fabrics with the swelling polymers to form a breathable barrier

material that can respond rapidly to chemical hazards. I explore the barrier properties

against an aerosolized liquid (the state most persistent CWAs are when dispersed)[7,54] and

the breathability of water vapor passing through the fabric. Finally, I wrap up the work

with conclusions I derived through this work and some additional work that could extend

this thesis and develop these materials further.

CHAPTER 2

STIMULI-RESPONSIVE MICROCRACKS IN PRICKLY PEAR CACTI

2.1 Introduction

Self-regulating membranes that adjust mass transfer in response to environmental stimuli have a wide range of potential applications that include thermoregulation,[55] drug delivery,[56,57] chemical synthesis,[58] and energy conversion (e.g., fuel cells).[59,60] Many such smart membranes occur in nature and some have provided inspiration for their synthetic counterparts.[60] In particular, Park et al.[60] have created a wax nanocrack-regulated self-humidifying membrane based on inspiration from the vapor transport regulation by stomata in cactus surfaces. To minimize water loss in harsh desert conditions (temperatures up to 63 °C and no rainfall for months[61–63]), this family of plants (i.e., Cactaceae) exhibits a unique form of photosynthesis that occurs during the day without respiration, while gas exchange occurs through opening of the stomata at night[64] (when temperatures are lower and the humidity is higher).[65,66] In addition to the 10 to 50 μm pore-like stomata,[67] after the first dry season the surface of *Opuntia* cactus cladodes (i.e., flattened, photosynthetic stem segments) develop a network of surface micro-fractures in the epicuticular wax that is a direct natural equivalent of the synthetic membrane developed by Park et al.[60] (see Figure 2.1).[68,69] Furthermore, as with the morphology of its synthetic equivalent, the shape of the micro-fractures is not static, but as I show in optical profilometry scans in Figure 2.1, changes dependent on the seasonal hydration state of the plant. As dehydration can reversibly decrease *Opuntia* pad volume by up to 60%, corresponding to a 30% decrease in area, the micro-fracture shape-change between wet and dry seasons can be substantial. While it is known that these wax micro-fractures

8

do not contribute significantly to the overall stomata-dominated transpiration of

Opuntia,[66] the substantial shape-change and potential translation into biomimetic

membrane design make the hydration-dependent morphology of the *Opuntia* surface

interesting. Accordingly, in this work I quantify how the macroscale hydration state

impacts the microscale morphology of the fracture network through dehydration and

surface characterization experiments. Based on these experimental results, I also

theoretically estimate seasonal variation of vapor transport across the micro-fracture

network.
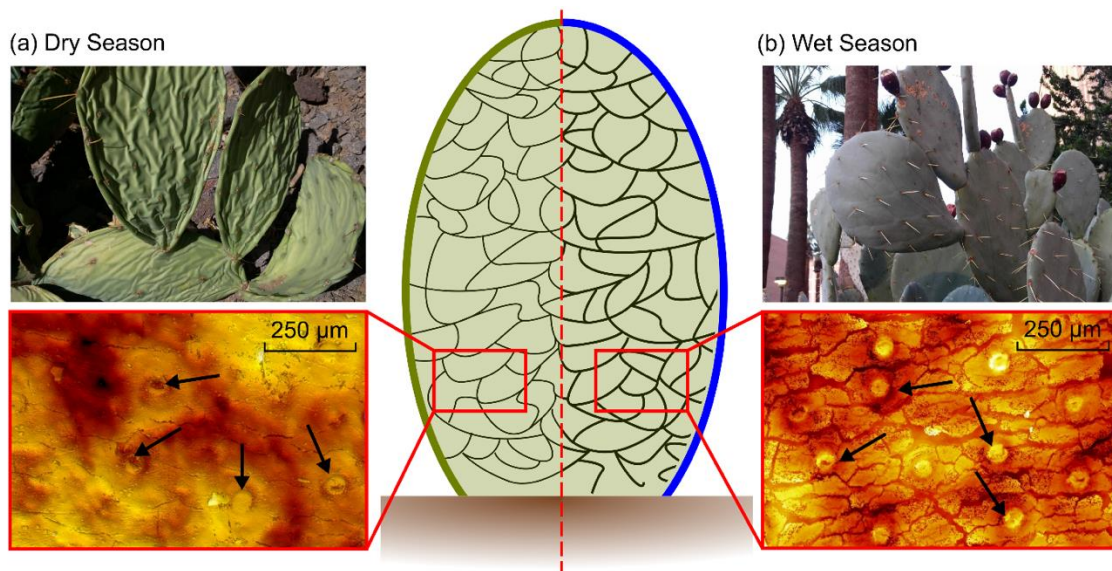
Figure 2.1. Schematic representations highlighting the crack structures (i.e., waxy cuticle) on the cactus epidermal surface of a (a) dehydrated sample and (b) hydrated sample of *Opuntia engelmannii*. The plants' physical macroscale structures are shown above the microscale optical profilometer scans, which highlight the changing micro-fractured wax morphology. In the profilometry images, black arrows indicate the location of stomata on the surface of the cacti.

2.2. Methods

2.2.1 Sample collection

To collect data representative of highly hydrated and dehydrated plant states, I harvested cladodes of *Opuntia engelmannii* on the Arizona State University Tempe campus during March and June of 2018. Due to seasonal winter and spring rainfall, in March the cacti have absorbed large quantities of water and are visibly swollen (see image in Figure 2.1b). In contrast, in June temperatures are typically above 40 °C with relative humidity below 10%, which leads to significant loss of water and visible shrinking of the cacti (see Figure 2.1a). In both cases, to ensure that the cladodes were at least a season old, I used new growth of buds and cladodes as age markers. The cladodes were taken to a nearby laboratory and tested immediately after harvesting.

2.2.2 Accelerated cladode dehydration measurements

After harvesting of the cladodes, I removed a 2 cm by 2 cm rectangular surface section using a stainless-steel razor blade. I gently rinsed the outside of these sections with deionized water to remove any dust and quickly dried them using nitrogen gas. To accelerate the dehydration process, I carefully reduced the thickness of the samples to approximately 1 mm. I allowed the dehydration to occur naturally through exposure of the bottom side of the cactus to an environmental chamber, which was maintained at 20 ˚C ±2 °C and a relative humidity of 30-40%. To quantify the dehydration rate, I weighed the samples on glass slides every 10 minutes using a 0.1 mg precision balance (Mettler-Toledo). Over the same timeframe, I measured the static contact angles of the samples every 30 minutes using Ramé-Hart 290 goniometer (6 drops per data point). I continued

the dehydration of the samples until 50% of the weight of the sample was lost. At such

conditions, *Opuntia* frequently die in the wild.[70]

2.2.3 Optical profilometry of the surface

To directly measure the morphological changes on the cactus surface, I used a

ZeScope optical profilometer. I used a 20x objective lens and stitched a composite image

with 40% overlap between images to measure an approximately 1 x 1 mm^2 area on the

cactus. I also attempted an *in-situ* measurement of the change in crack shape, but after

extended exposure the high intensity light the sample began to soften and the light visibly

reshaped the waxy surface. To ensure that the visible micro-fractures are indeed only in

the exterior wax (i.e., not in the underlying surfaces), I washed away the epicuticular wax

using dichloromethane and imaged the surface structure to see if any fractures remained.

As expected, after the solvent wash the surface surrounding the stomata was smooth (no

fractures were observed).

To systematically quantify the morphological characteristics of the cactus surface, I

developed a custom code in MATLAB which extracted linear profiles across the micro-

cracks manually selected by the user (see Appendix A for detailed coding). By selecting

multiple points within each identified crack, average crack profiles can be determined to

measure width and depth of the fractures. Using this approach, I analyzed over 300

fracture profiles.

2.3. Results and discussion

2.3.1 Hydration dependent epidermis micro-fracture morphology

I quantified the hydration-induced micro-fracture network morphological changes using macroscopic wettability measurements during controlled dehydration experiments and using direct microscale imaging of plants harvested during wet and dry seasons. First, I harvested highly hydrated cladodes (see image in Figure 2.1b) and periodically measured their surface water contact angle during slow, controlled dehydration. The plot in Figure 2.2a shows that as the cladode gradually loses about half its weight through water loss, the contact angle rises from just under 90° to just over 100°. The Cassie-Baxter model for the apparent contact angle of a composite surface, θ^*, can be used to estimate the average micro-fracture shape-change corresponding to this wettability increase.[71] Specifically,

$$\cos \theta^* = f_1 \cos \theta_1 + f_2 \cos \theta_2 \qquad (1.1)$$

Where f is the fractional area and θ is the contact angle of the micro-fractures (subscript 1) and the epicuticular wax (subscript 2). Since air gaps under water droplets are unlikely to form in the relatively shallow fractures, I can assume that $f_1 = 1 - f_2$. Based on previous work, the bottom of the fissures is highly hydrophilic[69] with $\theta_1 \approx 30°$, while the epicuticular wax static contact angle can be assumed to be hydrophobic with $\theta_2 \approx 110°$.[69] Using these values, I calculate the fractional area of the micro-fractures to be about 28% for the hydrated state with $\theta^* \approx 90°$, and 14% dehydrated for the state with $\theta^* \approx 100°$, respectively. I note that this hydrated state coverage estimate agrees well with the previous estimation of micro-fracture cladode coverage.[69] If I assume that the number of micro-fractures remains constant, the calculated fractional area change implies that the

12

average micro-fracture width decreases by about 50% when seasons change from wet to dry.

To directly measure microscale morphological differences between naturally hydrated and dehydrated cladodes, I used optical profilometry to scan cladodes harvested in the Spring and in the Summer (see images Figure 2.1). I note that my evaluation of the hydration state of these plants was rather qualitative, and I assumed them to be representative of fully hydrated and dehydrated states. In both states, optical profilometry confirmed the presence of the micro-fracture network. Based on the analysis of a 4 mm^2 area of optical profilometry images, the histogram in Figure 2.2b shows that average micro-fracture width decreases from about 15 µm ± 3 µm in the fully hydrated samples down to about 6 µm ± 1.9 µm (68% confidence interval) in the dehydrated state. Considering the qualitative evaluation of the naturally harvested plant's hydration state, this 60% reduction in the average exterior width micro-fracture agrees reasonably well with my 50% estimate based on contact angle measurements and Cassie-Baxter model.
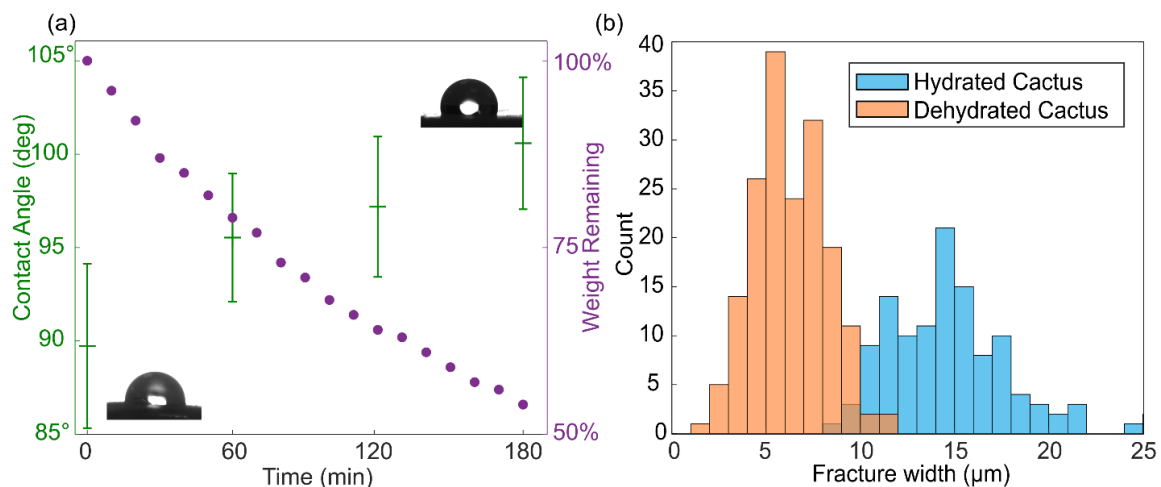
Figure 2.2. (a) The change in the water contact angle during controlled dehydration of a freshly cut cladode, and (b) histograms of micro-fracture exterior widths extracted from optical profilometry images of naturally hydrated and dehydrated cladodes.

13

2.3.2 Theoretical estimates of vapor transport across the micro-fracture network

Detailed characterization of the cross-sectional profiles of the micro-fractures also enabled us to theoretically estimate the effect of the micro-fracture shape change on moisture transport by simulating two idealized micro-fracture geometries. Specifically, the representative cross-sectional profiles across several micro-fractures (see Figure 2.3a) show that their geometry can be broadly assumed to vary between channels with rectangular cross-sections that can be solved analytically with a 1D assumption and more complex trapezoidal cross-sections requiring more complicated diffusion models (see Figure 2.3b). The optical profilometry experiments revealed that while the widths of the fractures change, their average depth remains constant at about 5 μm, regardless of the level of hydration. In addition, I measured the average distance between fissures as about 50 μm, which I took into account by modeling a "unit cell" with of single micro-fracture with flat areas extending from the micro-fracture to provide the correct spacing. The unit cell was then constrained by symmetry boundary conditions on both the sides. I modelled the areas surrounding the fractures as well as their edges as impermeable, while I assumed the mass transfer through the boundary layer above the cactus surface to be purely diffusive. I used the water vapor transport module in COMSOL Multiphysics 5.3a to simulate steady-state total moisture flux of the idealized bounding rectangular and trapezoidal one-dimensional channel geometries with an external width of 0.5 μm to 25 μm (the bottom width of the trapezoidal channel was assumed to be constant at 0.5 μm).

14
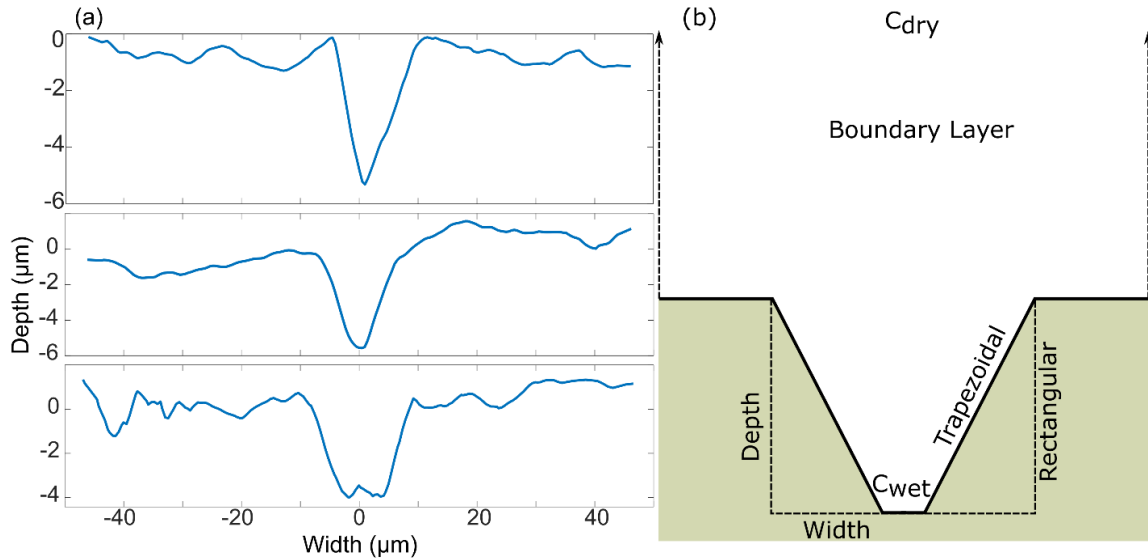
Figure 2.3. (a) Representative line profiles of surface micro-fractures showing the variety of channel types and (b) corresponding idealized system that was modeled to define the vapor transport out of the surface fractures.

By simulating the idealized bounding shapes defined in Figure 2.3b, I estimated the potential range of vapor transport modulation with micro-fracture shape-change. For ease of comparison, in Figure 2.4 I normalized the finite element method (FEM) results against the steady-state mass flux for a rectangular channel with width of 25 μm. According to the results, the vapor flux across the rectangular channels can increase by 570% if the external width changes from 0.5 μm to 25 μm. In turn, for the equivalent external width change of the trapezoidal channels with a fixed bottom width of 0.5 μm, the vapor flux can increase by 260%. To estimate how the overall vapor transport across the micro-fracture network is modulated by the hydration state of the plant, I numerically integrated measured hydrated and dehydrated micro-fracture size distributions with the width-specific vapor fluxes obtained from the FEM simulations. I performed this numerical integration for the two bounding geometries (rectangular and trapezoidal) to

15

estimate the change in the vapor transport from the "hydrated" state to the "dehydrated" state. Based on these results, I estimate that the vapor transport across the entire network decreases by between 22% (trapezoidal channels) to 30% (rectangular channels) as the micro-fractures average width decreases from 15 μm in the hydrated state to 6 μm in the dry state. Consequently, the plant-hydration-dependent surface morphological changes induce a moderate vapor permeation modulation of the micro-fracture network but cannot be considered to have an on/off type of response.
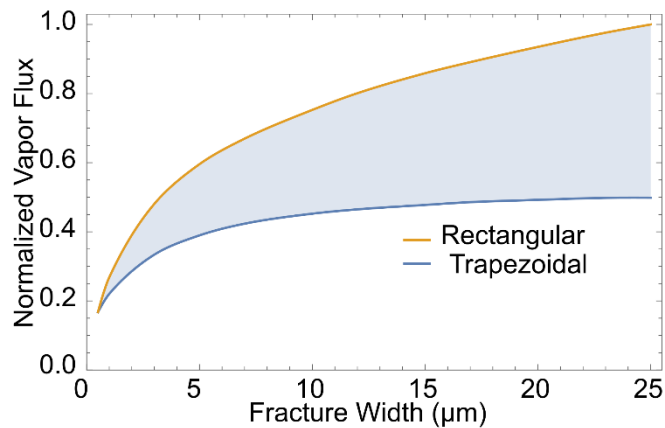
Figure 2.4. FEM simulation results showing the relative vapor loss rates based on the exterior width of the idealized rectangular and trapezoidal cross-section one-dimensional wax micro-fractures.

2.4. Conclusions

In this work, I demonstrated that seasonal hydration state of the *Opuntia* cactus induces reversible and significant morphological surface changes. In terms of wettability, the water contact angle of the cactus surface increases from 90° to above 100° as the hydration of the sample changes from fully hydrated to near fatally dehydrated. This change stems from shrinking of the deep micro-fractures in the hydrophobic surface of the cactus. Based on optical profilometry of cladodes harvested in dry and wet season, the

external width of these micro-fractures decreases from approximately 15 μm down to 6

μm, but their average depth remains fixed near 5 μm. By modeling vapor transport across

idealized rectangular and trapezoidal fractures, and integrating these results with

measured micro-fracture widths, I can estimate that dehydration can decrease the vapor

transport across the micro-fracture network by 22 to 30%. Consequently, the plant-

hydration-dependent surface morphological changes induce a moderate vapor permeation

modulation of the micro-fracture network but cannot be considered to have an on/off type

of response. Nevertheless, these fissures act as secondary vapor pathways, which creates

a hierarchical design to mediate water vapor loss from the surface. While in the *Opuntia*

cactus, this secondary pathway has a minor contribution as compared to the stomata,

achieving superior functionality through hierarchical design is one of the principle

biological strategies observed in nature.[72] Consequently, this hierarchical design could be

adapted from nature to produce multi-stimuli responsive membranes to guide complex

membrane mass transfer regulation.

CHAPTER 3

DEVELOPMENT OF A NON-ELECTROLYTIC SELECTIVELY

SUPERABSORBENT POLYMER

3.1 Introduction

A variety of polymer gels with a broad range of swelling characteristics are utilized

for sorbtive applications in gas-gas, gas-liquid, and liquid-liquid separation systems. In

gas-gas separation, polymers are often implemented as swollen membranes,[73–75]

improving membrane selectivity while retaining high transfer rates through the barrier.

Specifically, the permeability of the membrane is increased by the expansion of the

membrane pores via the active application of liquids.[75,76] Addition of liquid to swell the

membrane can also increase the membrane throughput by absorbing the gas and

transporting it in the liquid phase.[77] Swelling membranes are also often implemented for

separation of liquid-liquid systems. Due to their ability to alter surface properties,[77–79]

hydrophilic[80,81] or hydrophobic[82] compounds can selectively pass through the swollen

membrane, providing unique solvent-solute interactions and aiding the separation. If

separation of organic liquids from water is required, swelling polymers can also be used

in bulk, rather than as a membrane, to capture one phase in the matrix. While capture of

water is possible using hydrogels,[78,79,83] removal of the less prevalent organic phase is

typically preferred. This can be achieved using, for example, hydrophobic fiber

networks,[84–87] carbon nanotube based sponges,[88,89] porous elastomers[90] and gels.

Naturally, materials that can take up significant (>5x its own weight) content of the

organic liquid are highly desirable. For example, Ono et al. presented a series of

organophilic polyelectrolytic gels that can be tailored to swell in different solvents

depending on their ionomeric constituents.[52,53] These polymers were shown to swell best in organic liquids with moderate dielectric constants, but had limited swelling with highly non-polar substances, such as alkanes. Another limitation of these polyelectrolytic gels stems from their interaction with water, which reduces their ionic dispersion causing the swollen structure to collapse.[91,92]

 In this Chapter, I build on work from Mamada et al. and Zhang et al.,[93,94] and describe the synthesis of an affordable non-electrolytic gel that swells significantly in a variety of organic solvents while remaining unaffected by the presence of water. Specifically, I synthesized non-ionic polymers comprised of an alkane chain backbone with a N-butyl-N-phenylamide pendant group. Due to its structure, the cross-linked polymer was expected to swell upon exposure to organic liquids of moderate polarity, while not taking up water. Further, the swollen polymer should not collapse in water as ion induced osmotic effects are absent. In addition to the effect of the new pendant group, the effect of the crosslinker density and its length on swelling was studied. Solvents covering a broad range of dipole moments, dielectric constants, and hydrogen bonding capability were examined.

3.2. Methods

3.2.1 Monomer synthesis

 N-butyl-N-phenylacrylamide was prepared in a one-step reaction of N-butylaniline (TCI, 98+%) with acryloyl chloride (Sigma 99.5%). Acryloyl chloride (0.51 g, 5.6 mmol) was added dropwise to a cold solution of N-butylaniline (1.00 g, 6.5 mmol), and trimethylamine (0.93 g, 9.2 mmol) in dry tetrahydrofuran (THF, 6.0 mL) under nitrogen.

Upon complete addition, the reaction was allowed to warm to room temperature and was stirred overnight. Reaction completion was confirmed by thin layer chromatography (TLC). Following reaction confirmation, the precipitated trimethylammonium salts were removed by filtration. THF was removed via rotary evaporation. The resulting oil was dissolved in dichloromethane and sequentially washed with 1% hydrochloric acid, 5% sodium carbonate, and deionized water to remove residual acryloyl chloride and trimethylamine. The organic phase was dried with magnesium sulfate and passed through a column of basic alumina. Upon loading the column, ethyl acetate was used to elute the product. Removal of the solvent via rotary evaporation resulted in a colorless oil (67% yield), which crystalized when stored at -20 °C. The purity of the product was estimated to be 99% based on hydrogen nuclear magnetic resonance spectroscopy (^{1}H NMR, 400 MHz). See Appendix B for NMR analysis details and spectra.

3.2.2 Polymerization

Poly(ethylene glycol) dimethacrylate (PEGDMA 200, Polysciences) and 2,2'-azobis(2-methylpropionitrile (AIBN) were added to a 3 M solution of the monomer in benzene. The amount of PEGDMA 200 was varied from 0.75 mol% to 2 mol% while the concentration of AIBN was held at 0.8 mol% (based on monomer). The reaction mixture was degassed with 3 freeze-pump-thaw cycles using nitrogen prior to polymerization. The polymerization was performed in a constant temperature bath overnight at 50 °C. After polymerization, the sample was removed from the glass container and washed overnight in a Soxhlet extractor with dichloromethane to remove any unreacted or non-crosslinked material. The sample was then dried in preparation for testing.

3.2.3 Polymer Characterization

Using a 0.1 mg precision balance (Mettler-Toledo), a small quantity of polymer was added to a scintillation vial and weighed before swelling. Following the ASTM D3616 – 95 standard, the samples were flooded with the chosen solvent and sealed for 16-20 hours before a swollen weight was recorded. The final weight was used to determine the swelling degree, *s*, which is defined as:

$$s = \frac{M_{swollen} - M_{dry}}{M_{dry}} \tag{3.1}$$

The polymer swelling was tested in dichloromethane (DCM) (Sigma, 99%), ethanol (KOPTEC, 200 proof), hexane (Sigma, 95+%), DI water, N,N-dimethylformamide (DMF) (Sigma, 99%), tetrahydrofuran (THF) (Sigma, 99%), 1,4-dioxane (Sigma, 98%) and *o*-xylene (Sigma, 99%). Swelling measurements were performed 3 times for each solvent. In addition to the single solvent swelling, 50:50 volumetric mixtures of water and THF, or *o*-xylene were tested.

3.3. Results and Discussion

3.3.1 Monomer and Polymer Synthesis

N-butyl-*N*-phenylacrylamide was prepared in 67% yield and ~99% purity in a single reaction step shown in Figure 3.1. The colorless to light yellow liquid was stable for several months when stored at -20 °C, without added radical inhibitor and crystallized on standing at this temperature.

The free radical polymerization, shown schematically in Figure 3.1b, was run overnight at 50 °C to ensure a high degree of polymerization. Polymerization was

considered successful when a firm gel was formed. Low molecular weight material was removed by extraction and solvent was subsequently removed via evaporation, yielding approximately 0.9 sol-gel fraction consistently. The polymer was a glassy, brittle solid in the non-swollen state. Multiple polymerizations were performed at crosslinker concentrations ranging from 0.75 to 2.00 mol% (based on monomer). Higher crosslinker concentrations showed minimal deviation in the measured swelling ratios, while at lower crosslinker concentrations the data was more variable.
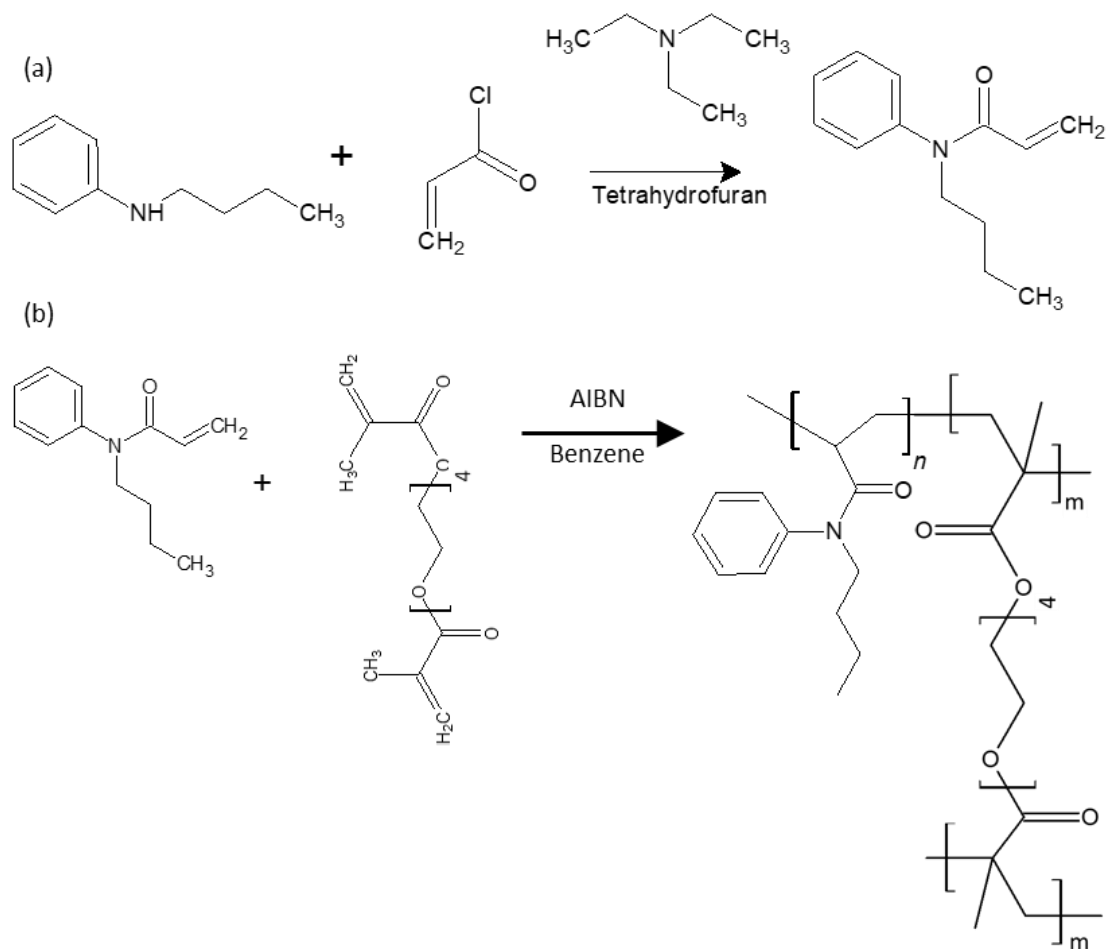
Figure 3.1. Reaction schematics for the reaction of (a) N-butylaniline with acryloyl chloride to produce the monomer and (b) the reaction of the monomer with the PEGDMA 200 to produce the homopolymer network.

3.3.2 Swelling behavior

Swelling tests revealed moderate to high swelling of poly(N-butyl-N-phenylamide) in a number of organic solvents, but a nearly negligible response to water. In the course of swelling, the polymer transitioned from a glassy solid to a sticky semi-swollen state and finally, a slippery swollen state. The mechanical strength of the polymer also changed significantly, with a large apparent decrease in elastic modulus as the swelling process occurred. Since the post-swelling mass measurement was conducted immediately after

removal of the sample from the liquid to prevent any artifacts due to evaporation, some

mass gain could be due to a thin liquid film on the polymer surface. To visualize liquid

uptake into the bulk of the polymer, swelling experiments were conducted in water dyed

with methylene blue. The same polymer sample was subsequently submerged in a

solution of KEDA royal blue dye in THF. As seen in Figure 3.2, the polymer had no

observable blue coloration after soaking in the water solution, while after soaking in THF

the polymer had clearly taken up the dye.
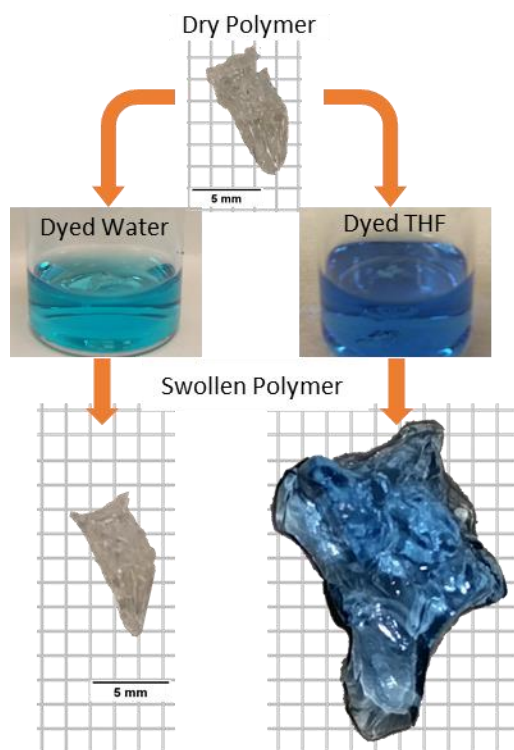
Figure 3.2. The polymer swelling in dyed water and THF. The top image shows the dry polymer before a 24 h soak in dyed solvent, the middle images show the polymer submerged in water (left) and THF (right), and the images on the bottom show the same polymer after removing it from the water (left) and the THF (right). The experiments were done sequentially using water first, drying the polymer, and then adding it to THF so the same piece of polymer was used in both experiments.

The degree of swelling was highly dependent on the liquid and crosslinker content. Polymer prepared with a crosslinker concentration of 1% swelled up to 33 mL/g in THF. Similarly, dichloromethane, *o*-xylene, and 1,4-dioxane swelled between 20 and 24 mL/g. Exposure to hexane, DMF, ethanol, and water caused little swelling, gaining only 1 to 4 mL/g. The observed swelling behavior in the different solvents is similar to that found for polymers synthesized by Ono et al.[52] In addition, as in the case of Ono work, there is no evident correlation between the degree of swelling and Hansen solubility parameter (δ) or surface tension of the solvent (see Figure 3.3a and 3.3b).

The Hansen solubility parameters for a given solvent are defined as the square root of the combined cohesive energies including dispersion, intermolecular and hydrogen bonding energy. The noncombinatorial free energy ($\Delta G^m_{noncomb}$) is given by:

$$\Delta G^m_{noncomb} = \varphi_1 \varphi_2 V (\delta_1 - \delta_2)^2 \tag{3.2}$$

With φ_1 being the volume fraction of the polymer and φ_2 being the solvent volume fraction, V is the total volume of the mixture, and δ_1 and δ_2 are the Hansen combined solubility parameters for the polymer and solvent, respectively. The free energy of swelling a polymer (ΔG_{swell}) is given by:

$$\Delta G_{swell} = \Delta G_{stretch} + \Delta G_{mix} \tag{3.3}$$

Where $\Delta G_{stretch}$ is the free energy of stretching the polymer and ΔG_{mix} is the free energy of mixing the polymer and the solvent.[95] Absorption requires a negative free energy of mixing. When this condition is met, the polymer network will expand until the favorable interaction between the solvent and the polymer is offset by the energy cost of polymer expansion. The ΔG_{mix} can be expressed in terms of the noncombinatorial free energy of mixing ($\Delta G^m_{noncomb}$) and the combinatorial entropy change of mixing (ΔS^m_{comb}):

$$\Delta G_{mix} = \Delta G_{noncomb}^m - T \Delta S_{comb}^m \qquad (3.4)$$

Patterson et al. found that $\Delta G_{noncomb}^m$ was equivalent to the change in enthalpy on mixing (ΔH_{mix}).[96] The condition for absorption can then be defined as:

$$\Delta H_{mix} \leq T\Delta S_{comb}^m - \Delta G_{stretch} \qquad (3.5)$$

where T is the temperature. The value of the right side of the equation is not known for this polymer system, but it nonetheless demonstrates that a threshold value of ΔH_{mix} is required for absorption to occur. The value of ΔH_{mix} can be expressed as:

$$\Delta H_{mix} = U_m - (U_1 x_1 + U_2 x_1) \qquad (3.6)$$

where U_m, U_1, and U_2 are the internal energies of the polymer-solvent mixture, the polymer, and the solvent, and x_1 and x_2 are the mole fractions of polymer and solvent in the mixture, respectively. When expressed in terms of cohesive energy density ($\mathcal{E}$) the expression becomes:

$$\Delta H_{mix} = [\mathcal{E}_m - (\mathcal{E}_1 \varphi_1 + \mathcal{E}_2 \varphi_2)]V_m^m \qquad (3.7)$$

where V_m^m is the molar volume of the mixture. The $\mathcal{E}$ in Equation 3.7 can, in turn, be expressed as sums of dispersion, intermolecular (principally permanent dipole-dipole interactions), and hydrogen bonding terms.[97] The solvent cohesive energy density can be estimated using the equation:

$$\mathcal{E}_2 = (\Delta H_{vap} - RT)/V_m^s \qquad (3.8)$$

where ΔH_{vap} is the change in enthalpy of vaporization and V_m^s is the molar volume of the solvent. Changes in $\mathcal{E}_m$ relative to $(\mathcal{E}_1 \varphi_1 + \mathcal{E}_2 \varphi_2)$ are due to changes in the number and strength of these interactions. Cases where the strength of these interactions in the mixture is reduced relative to those in either the pure polymer or solvent will disfavor absorption. It is therefore reasonable to expect that strong absorption would occur at

26

intermediate ϵ_2 values while being inhibited for solvents with large self-interaction energies as well as those with insufficient interaction energies with the polymer to compensate for the loss of favorable polymer self-interactions on swelling.

A plot of the degree of swelling as a function of ϵ_2 is shown in Figure 3.3c. The absorption goes through a maximum at a ϵ_2 of ~0.4 kJ cm^{-3} and indicates that there should be reasonably high absorption for ϵ_2 values ranging from 0.3-0.5. This range covers a large number or organic liquids. The striking similarity between the ϵ_2 and dielectric constant (see Figure 3.3d) plots suggests that the dielectric constant is also a potentially useful metric for predicting absorption.
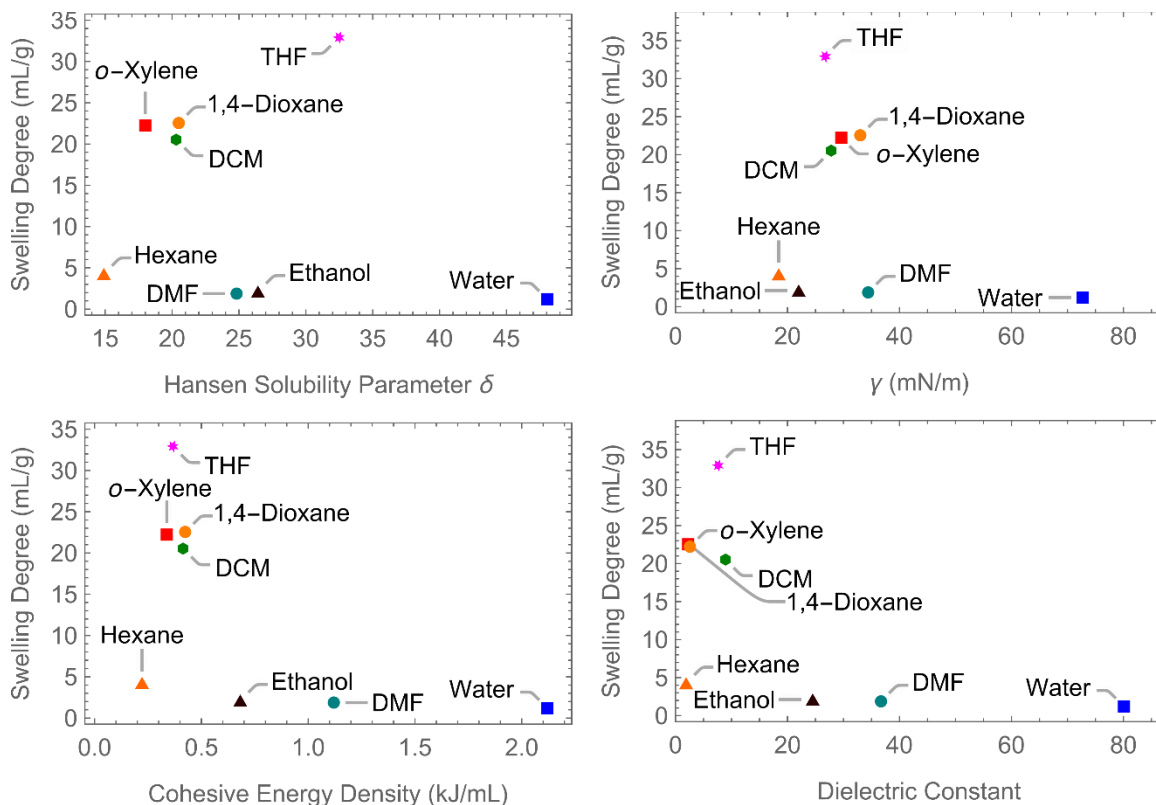
Figure 3.3. Solvent swelling ratios after 20-hour submersion 1% crosslinking density vs. solvent property (a) Hansen solubility parameter, (b) Surface tension, (c) Cohesive energy density, and (d) Dielectric constant.

In addition to characterizing the swelling by the thermophysical properties of the solvents, the effects of crosslinking density and the crosslinker length on the swelling ratio were also studied. Figure 3.4a shows that the swelling ratio in dichloromethane did not change significantly for crosslinker concentrations between 1.5 to 2.0% (based on monomer). Below 1.5%, the absorption capacity increased with decreased crosslinker percentages, culminating in a value at 0.75% that was over twice that of the higher crosslinker percentages. Lower crosslinker concentrations resulted in material that broke apart on swelling. Even at a crosslinker concentration of 0.75%, light contact with the swollen polymer tore off small pieces of material.

To study the effect of the length of the crosslinker on the swelling ratio, Poly(ethylene glycol) dimethacrylate (PEGDMA) with PEG weights of 200, 400, and 1000 Da were incorporated at 1.25 mol% (based on monomer). The PEG molecular weights correspond to an average of 4.5, 9, and 23 ethylene glycol repeat units, respectively. The effect of the crosslinker length on swelling is shown in Figure 3.4b. On increasing the crosslinker length the swelling drops in solvents like THF, *o*-xylene, and dichloromethane by as much as 40%. This suggests that using a shorter crosslinker or changing the chemistry of the crosslinker could significantly improve the swelling using the same monomer. However, multiple attempts to utilize ethylene glycol dimethacrylate as the crosslinker were unsuccessful, gels were formed in only 2 out of 25 attempts. It is believed that the single unit crosslinker resulted in too much steric hindrance for efficient coupling between polymer chains to occur. In future work I will evaluate cross-linkers

28

with 2-3 ethylene glycol repeat units or replace the ethylene glycol with an alkanediol of similar length.
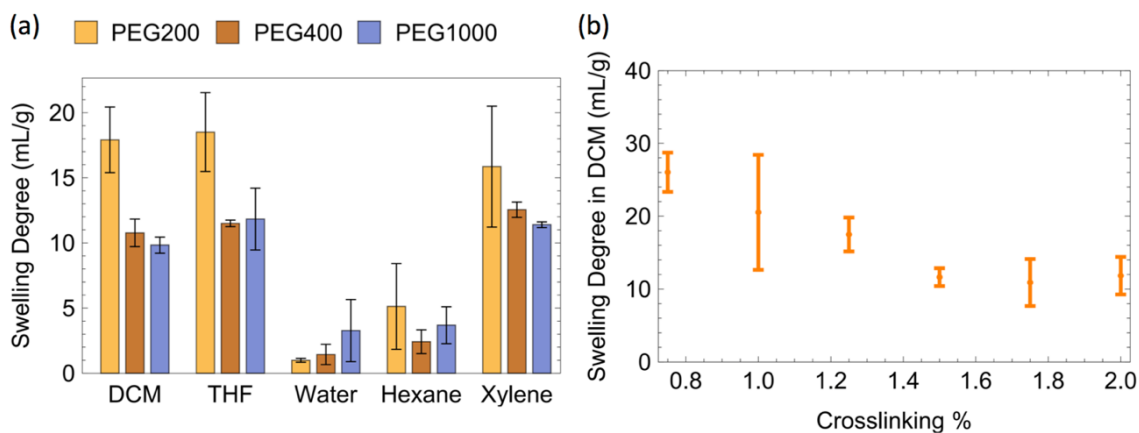
Figure 3.4. (a) Swelling of select solvents with the PEG200 dimethacrylate, PEG400 dimethacrylate, and PEG1000 dimethacrylate crosslinkers with standard deviations and (b) Swelling in dichloromethane at different crosslinking percentages with one standard deviation indicated.

3.3.3 Selective Absorption

To explore how the polymer reacts in the presence of water and saline (1 M sodium chloride), xylene/water and xylene/saline emulsions were generated and maintained during swelling to measure the swelling ratio. The emulsion was maintained by stirring the two phases to prevent phase separation. Figure 3.5 shows the progression of absorption of a xylene emulsion where the organic phase was colored with Oil Red dye. The ultimate swelling ratio was largely unaffected by the presence of the water or saline, with both pure *o*-xylene and the emulsion resulting in a swelling ratio of 20 mL/g.
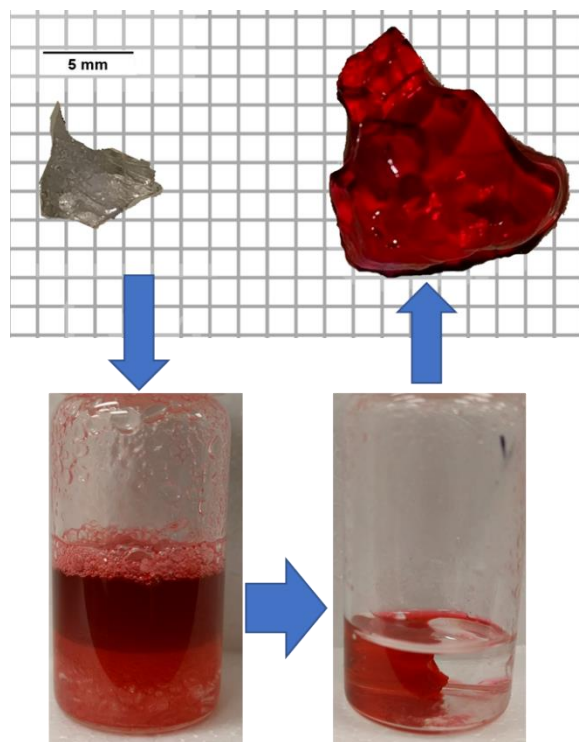
Figure 3.5. Polymer swelling in emulsified *o*-xylene (dyed red) and water. A polymer chip before swelling (upper left), is added to the emulsified liquids for 24 hours (lower left). After 24 hours, additional unabsorbed xylene was removed, and the polymer was left in the aqueous phase only (lower right) and removed to be imaged and massed (upper right).

The ability for this polymer to absorb miscible liquids like THF in water was also tested. While highly swelling in pure THF, as shown in Figure 3.3, a solution of 50% THF in water showed no appreciable swelling after 24 hours. It is likely that the chemical potential of the THF was sufficiently changed by the water that it was no longer energetically favorable for it to enter into the polymer matrix. There may be miscible water-solvent systems that at least partially swell the polymer. Additional tests will need to be run to determine what levels of miscible water are tolerable to maintain swelling properties.

3.4. Conclusions

This work has shown that non-electrolytic gel networks can maintain moderate to high swelling degrees for solvents covering a range of cohesive energies and dielectric constants. The minimal interaction with water for these polymer gels, shown by absorbing xylene from a water emulsion, highlights that they are also candidates for organic liquid uptake even in aqueous environments. While the THF-water blend did not achieve any swelling, it is worth exploring if partially miscible liquids such as the azeotrope of water and ethyl acetate would be able to be absorbed.

Based on the crosslinker length study, the increasing length of the ethylene glycol linker is detrimental to the swelling in high swelling solvents. An alternate crosslinker like an alkane-diol diemethacrylate might provide better results while avoiding the steric issues associated with this monomer. Additionally, a small percentage of a comonomer with less steric hindrance may permit the use of a short crosslinker, such as ethylene glycol dimethacrylate.

CHAPTER 4

BREATHABLE, STIMULI-RESPONSIVE, AND SELF-SEALING CHEMICAL

BARRIER MATERIAL BASED ON SELECTIVELY SUPERABSORBING

POLYMER

4.1 Introduction

The occasional use of chemical warfare agents (CWA) by rogue states in current

conflicts provides a reminder that these hazards are a real threat and not a century old

warfare relic.[98] Although hazmat suits made of fully impermeable barrier materials

provide an effective means of protecting against CWAs, their extended use presents

another challenge to the user. Specifically, the hazmat suits also prevent water vapor

transport and thus inhibit evaporative cooling. As a result, even moderate exertion in a

temperate climate can cause hyperthermia in as little as 45 minutes.[10,23] To extend the

safe working time, active cooling systems must be worn under protective

clothing.[10,12,18,19,99,100] Unfortunately, such systems are heavy, require batteries, and are

often not readily available in field conditions where CWA threats exist. This conundrum

has motivated a search for novel materials that allow water vapor but not CWA

permeation. So far, several such selective barrier membranes based on carbon

nanotubes,[32,33] graphene oxide flakes,[4,5] and selective polymers[3,34,35] have shown promise

in protecting against CWA penetration while allowing some water vapor transport. For

many of these fabrics the degree of breathability is typically around or mildly above the

breathable fabric threshold of 2000 gm^{-2} per 24 hours,[24] which allows for an equivalent of

about 100 W of evaporative cooling of a fully covered typical adult (~ 2 m^2 of clothing).

This cooling rate only addresses metabolic heat generation of an idle individual that is not

experiencing environmental heating.[25] Thus, many of the fabrics provide too low of a degree of breathability to be worn for extended periods of time during operations in hazardous areas. For the few cases of the protective fabrics that have higher breathability, the material cost is currently a challenge for their deployment.

Here I propose an alternative approach to extend operational time in hazardous environments that is based on a highly breathable composite fabric that self-seals only when exposed to target chemicals. This approach is based on the use of selectively super-absorbing polymer (SAP) micro-beads dispersed on a highly breathable fabric. Many CWAs, especially nerve and blistering agents, have low vapor pressure[7] and can only be dispersed as a "fog" via aerosolization. The proposed SAP micro-bead functionalized fabric would seal on contact with an organic aerosol, preventing its penetration (Figure 4.1). In contrast, the fabric would remain porous on exposure to water, allowing its vapor to pass. In this work, I demonstrate the feasibility of this approach and show that a balance between high breathability under normal conditions, and the ability to completely stop an organic aerosol, can be achieved.
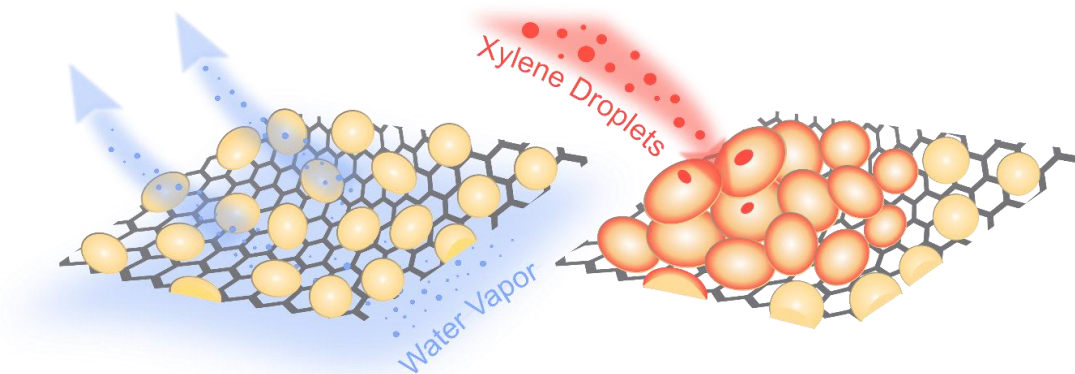
Figure 4.1. Schematic of a sealable fabric system that allows water vapor to freely move through the material while hazardous organic droplets are absorbed by the SAP microparticles, blocking their transport.

4.2 Methods

To demonstrate the selectively self-sealing fabric concept, I utilized the SAP, poly(N-butyl-N-phenylacrylamide), discussed previously.[101] The polymer swells in a range of organic solvents but only negligibly in water (see Chapter 3 for details). However, the material used in this study was cross-linked with 1,10-decanediol dimethacrylate (Sigma, 97%). The polymerization reaction was done in bulk using 0.5 mol% crosslinker (relative to monomer) using 0.8 mol% 2,2'-azobis(2-methylpropionitrile) (Sigma, 98%) as the initiator. The reaction was run for 24 hours in a stirred water bath at 50°C. The resulting polymer was washed in dichloromethane to remove any poorly cured product, resulting in a gel fraction of 0.87. After washing the polymer, a fraction was tested to ensure that it remained highly swelling in o-xylene, a representative organic liquid. Specifically, the swelling degree, defined as the ratio between the volume of liquid captured per mass of dry polymer, remained around 22 ± 0.9 mL/g as shown in Chapter 3. I selected o-xylene because it has a vapor pressure similar to some threat agents of interest (i.e. is likely to

remain an aerosol when dispersed)[7,54] and is predicted to have similar swelling properties

to that of agents like Soman and Sarin based on their cohesive energy density.[7]

After synthesizing the bulk polymer, I used a mortar and pestle to grind the material

into a powder. Next, I sieved the powder through 60 μm nylon mesh (Elko Filtering).

Using optical microscopy (Appendix C) I determined the particle distribution to have an

average effective diameter of 44 ± 19 μm. To complete fabrication of the membranes, I

dispersed the SAP particles onto a nylon mesh with 40 μm openings that covered 34% of

the area. I selected this mesh because it provides water vapor permeability equivalent to a

typical cotton t-shirt, but it does not absorb o-xylene (i.e. any swelling and sealing effects

stem from the SAP).

To determine the ability of the SAP micro-bead coated mesh to seal upon o-xylene

aerosol exposure, I built a custom testing setup. In it, I generated the aerosol using a 1.7

MHz piezoelectric fog generator (Amazon) in an in-line vessel which resulted in a

headspace densely packed with xylene droplets (see image in Figure 4.2a&b). According

to Donnelly et al.,[102] I can estimate the size of the droplets based on intrinsic properties of

the liquid. Specifically, using the properties of o-xylene, I can estimate the average

droplet size by the following equation:

$$d = 2\pi c_1 \left(\frac{\sigma}{\rho}\right)^{\frac{1}{3}} \left(\frac{2}{\omega}\right)^{\frac{2}{3}} \tag{4.1}$$

Using $c_1 = 0.35$, that is a fitted value for o-xylene (considering it an inviscid fluid),

surface tension of $\sigma = 30$ mN m^{-1}, density of $\rho = 878$ kg m^{-3}, and frequency of oscillation

of the piezoelectric element $\omega = 1.70$ MHz, I calculated that the aerosol droplets had an

average diameter of 8 μm (0.27 pL). This droplet size is appropriate for testing since it corresponds to the range expected for many dangerous aerosol fogs.[54]

The nylon test membranes were placed between two glass joints (inner diameter of 26.8 mm), using a Viton O-ring (inner diameter of 37.7 mm) to create a seal between the exposed side of the membrane and the glass joint. I dispersed a known mass of the SAP powder onto the nylon mesh and spread it over the area inside the O-ring diameter by vibrating the sample on a flat surface by hand. Notably, I created a separate fabric sample for each individual experimental run. Subsequently, I inserted the coated mesh into the glass joint and clamped it in place. The dense *o*-xylene fog that was generated using the piezo was carried by a 400 sccm nitrogen sweep towards the target membrane. To measure the penetration of o-xylene, an activated carbon bed was used as a trap for any organic material that passed through the membrane (see Figure 4.2a&b). The carbon bed was periodically removed and rapidly weighed to measure the mass gain of o-xylene and replaced into the apparatus.

Additionally, to avoid building up a large pressure gradient, I installed a small vent next to the sample exposure area. This alteration provided the sample with consistent exposure to the aerosol. From unobstructed aerosol flow content, I found that the mesh samples were exposed to 199 g m^{-2} min^{-1} of *o*-xylene. This exposure level corresponds to a dense fog estimated to contain 280 g m^{-3}; far greater than the 0.5 g m^{-3} found in most natural fogs.[54,103] Consequently, this high density aerosol flow likely represents an extremely high loading of CWA and a "worst-case" scenario for exposure. We elected this "worst-case" testing over more dilute fogs because we expect the SAP to rapidly take up dilute fogs.

36

While larger SAP chunks require minutes to hours for the bulk of the swelling to occur (see Appendix B for details), for the ~40 μm sized particles used in this study, a similar degree of swelling occurs on the order of 1 s (See Figure C2 for details). During testing, the SAP coated mesh (~ 59% packing density) is exposed to approximately 0.1 g min^{-1} of xylene. Given this packing density and loading, it would be expected that complete filling of the void volume should occur within 4 minutes. Further, due to rapid diffusion of the target liquid within the polymer, coupled with the high probability of adjacent particles coming into contact, localized swelling regions become redistributed throughout the matrix. The distributed swelling decreases the open area of the mesh and increases the probability of aerosol particle capture. Although lower exposure fluxes were not examined, it is our expectation that they should have a lower net breakthrough at equivalent exposure levels. The presented results would therefore represent a worst-case scenario relative to lower rates of exposure. Nonetheless, the examination of varying exposure rates on aerosol penetration are planned in future work.

4.3 Results and Discussion

The images in Figure 4.2a and b and the plot in Figure 4.2e show that addition of the SAP particles drastically reduces and even nearly eliminates *o*-xylene mass permeation through the mesh. Without any particles, the nylon mesh reduces the aerosol permeation rate from 199.4 to 35.4 g m^{-2} min^{-1} (i.e. blocks 80% of incoming aerosol). The addition of 0.3 g of the SAP particles (the equivalent of adding approximately 0.50 mm in bed height) reduces the *o*-xylene permeation rate down to 17.1 g m^{-2} min^{-1} (i.e. blocks 90% of incoming aerosol). In turn, addition of 0.5 g of the SAP particles (equivalent to a bed height of 0.76 mm) almost eliminates the *o*-xylene permeation rate, reducing it down to

37

0.43 g m^{-2} min^{-1} (i.e. blocks >99% of the incoming aerosol). The images of the pre- and post- o-xylene exposure of SAP-covered meshes, shown in Figure 4.2c, demonstrate the mesh sealing via the swollen polymer.

To separate the impact of swelling and geometrical blocking of the droplet, I also tested permeation of mesh covered with a 1 mm bed of similarly sized particles (average size of 37 ± 13 μm) of a polymer that does not swell in o-xylene. The permeation of o-xylene through the "mesh with 0.5 g of non-reactive polymer" is about the same as that of the mesh covered by 0.3 g of the SAP beads. Consequently, the near complete blockage of the mesh is not solely due to the physical presence of the particle bed but requires the additional swelling effect. I compared the permeation rates of the SAP bed to that of the NSAP bed and found that 97.5% of the o-xylene penetration was blocked relative to the latter sample. This suggests that added back pressure from the mesh and polymer bed that could drive more aerosol out the vent did not account for the majority of the stopping power of the SAP bed.
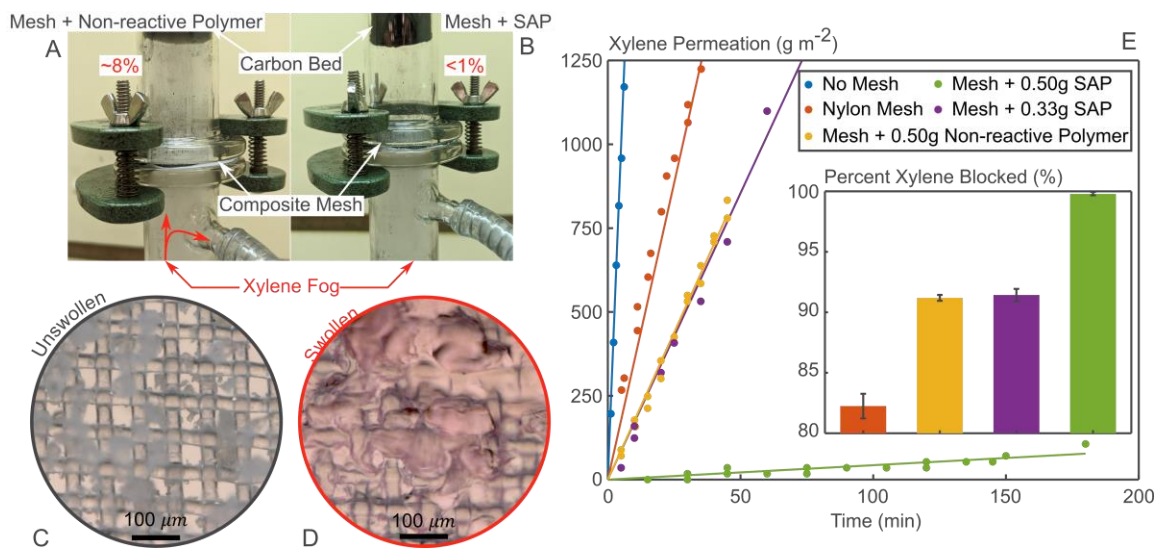
Figure 4.2. Images of experimental setup with *o*-xylene aerosol flow going through 0.5 g of (a) non-reactive polymer and (b) SAP covered nylon mesh. Microscopy images of SAP on the nylon mesh both before (c) and after exposure (d) to dyed *o*-xylene; (e) *o*-xylene adsorbed by the activated carbon trap including an inset corresponding to the percent permeation (relative to the total flow) for each scenario.

To determine the level of breathability provided by the self-sealing SAP-covered membranes, I measured their water vapor transport rate (WVTR), following the E-96 ASTM desiccant method.[104] I used meshes with and without the powders to cover a container with an opening of 31.3 mm in diameter. I placed an excess of calcium chloride (Millipore Sigma, 99%) desiccant in the container to desiccate the environment and thus created a water vapor sink with ~0% relative humidity. I placed the covered container in a controlled environment at a temperature of 33°C and a 100% relative humidity. I left the samples in this environment for 6 to 7 hours and periodically measured the mass change (Ohaus Explorer, 0.01g).

The plot in Figure 4.3 shows that for a 24-hour period, I see a $11,700 \pm 700$ g m^{-2} of water vapor permeation through the nylon mesh (i.e. a total mass transport resistance $R_{tot} = \Delta C / WVTR =$ 248 s m^{-1} for a water concentration difference, ΔC, of 0.0337 kg m^{-}

39

[3]). As expected, this permeation rate is comparable to one I measured for a thin cotton fabric. Remarkably, the addition of the 0.5 g of the SAP particles that nearly eliminated the organic aerosol permeation through the nylon mesh does not appreciably impact transport of water vapor through it (10370 ± 1400 g m^{-2} day^{-1} or R_{tot} of 281 s m^{-1}). This result affirms my assertion that I can maintain high levels of breathability prior to any exposure while achieving complete impermeability in the presence of hazardous stimuli.
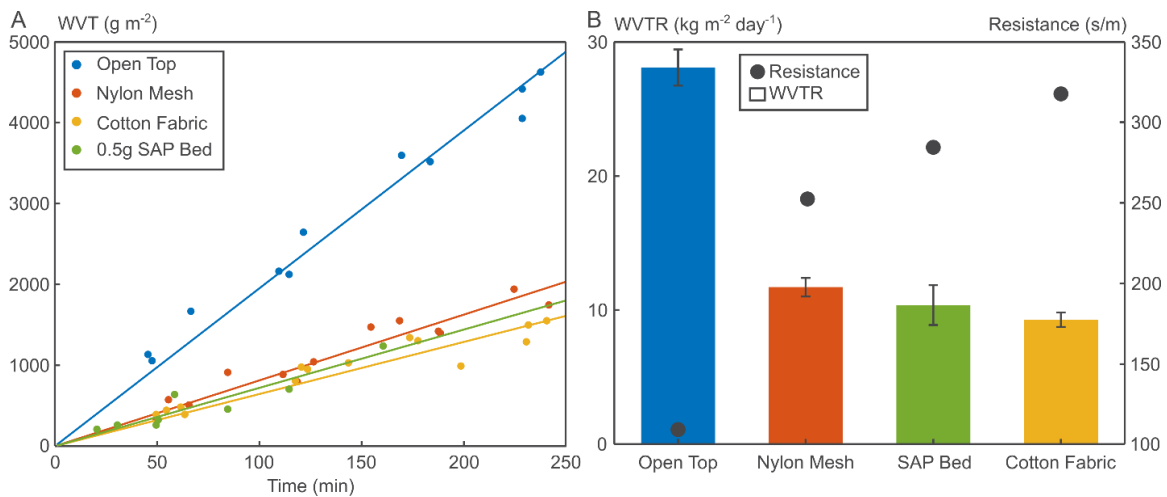
Figure 4.3. (a) Plot showing the water vapor transport (WVT) through the membrane as a function of time, (b) histogram of the water vapor transport rate (WVTR) and the resistance to permeation measured each sample.

4.4 Conclusions

In summary, in this Chapter I experimentally demonstrated that meshes covered with selective SAP particles can self-seal through swelling, and almost entirely eliminate organic aerosol permeation. Please note that synthesis of the SAP in particle form would

allow for more uniform distribution over the mesh or fabric, thereby likely eliminating any structural defects and completely blocking the aerosol. At the same time, the 1 mm thick micro-particle bed remained as breathable as a cotton shirt. Relative to other proposed breathable hazmat suit materials,[3–5,32–35] these initial results suggest that this approach will provide one of the highest levels of breathability. Specifically, the SAP-particle covered membranes provide comparable permeation to the graphene oxide films developed by Steinberg et al.[4] (based on their estimates, at 37°C, they expected about 10 kg m^{-2} day^{-1}) and the carbon nanotube film developed by Bui et al.[32] These materials have the obvious advantage of stopping not only aerosol but also vapor permeation, but at a substantially increased cost (thus might not be able to cover entire hazmat suit area). Consequently, an interesting scheme could include a combination of my concept with these approaches (e.g. some regions of the hazmat suit coated with SAP particles and some others with CNT films). The current work is a proof-of-concept of my approach. With improved synthesis of the SAP particles and rational multiphysics model-based design[105] I might be able to generate nanoparticle films that also prevent vapor permeation (albeit with a likely decrease in the water vapor permeation rate). In any case, this highly breathable protective material concept is a promising route toward extending operational time in areas where CWA threats exist and provides motivation for further development of SAPs and SAP-based protective fabrics. Lastly, since such polymers can be synthesized in large batches and dispersed using scalable approaches, the fabrication cost is unlikely to be prohibitive.

CHAPTER 5

CONCLUSIONS AND FUTURE WORKS

5.1 Main Findings

Chemically protective fabrics are potentially viable using swelling sealing polymers as a protective barrier. Through this work, I developed a new polymeric network that can swell highly and capture organic liquids. I explored how cactus wetting and shape change revealed shifting cracks that accounted for changes in vapor transport and surface wettability. And I combined these two works to create a composite fabric that provides high breathability to water vapor, but responds to stimulus (e.g. xylene fog) to swell and close the pore structures. I showed that combining these works provides a framework for this idea to be further explored and adapted to many other chemicals.

These works fundamentally rely on using chemical moiety interactions to induce mechanical deformation and create a stimulus driven shape changing material. I explored a biological barrier material with a similar shape change to augment breathability and showed that hydration levels in prickly pear cacti affect the microstructure of the surface wax to reduce dehydration rates. I was able to find that the macroscale properties, namely wettability, were able to be altered by relatively minor changes at the microscale. I specifically found that decreasing the total weight of the cactus by 40% reduced microfractures from 15 µm $\pm$ 3 µm in the fully hydrated samples down to about 6 µm $\pm$ 1.9 µm. While that reduction seems minor in absolute size, it changed the contact angle on the surface of the pad from ~90° to over 100°. That these minor mechanical

deformations manifest large macroscale change in properties provides guidance to creating a material to change its breathability and create a protective fabric.

Starting from acrylamide chemistry, I developed a polymer network that showed high swelling properties in a range of solvents. The swelling shows a rapid expansion upon initial exposure to a swelling liquid that diminishes with time. The rates of liquid uptake are suitable for use in breathable hazmat suit. By comparing different solvent parameters with the swelling ratios, I showed that the swelling can be anticipated based on the cohesive energy density of the solvent. This provides a metric by which to evaluate new materials and see if they will likely swell highly in poly(N-butyl-N-phenylamide). The observations I made in emulsified xylene-water mixtures highlight that absorption by the polymer does not depend on the presence of water or saline solution. This is an important distinction from previous electrolytic gels that rely on charge dispersion to remain in a swollen state. It also provides a basis to assume the polymer will be unaffected by the presence of water or perspiration; this is a critical requirement if I adapt this to articles of clothing.

Developing the material concept further, I explored using poly(N-butyl-N-phenylamide) in a composite fabric to test its sealing capabilities. With previous simulation work[106] it was expected that using polymer beads on the same size scale as the pore openings of the fabric would provide the most efficient capture of aerosolized material. Further, that work suggested that even as little as a monolayer of micron-sized particles could seal-off 95% of the pore area in well under a second. From my experimental work, I found that a monolayer was not enough to seal the fabric and avoid xylene from penetrating to the activated carbon bed. In fact, I found that a polymer bead

bed height of approximately 1 mm was needed to provide enough absorbing power to stop significant xylene penetration. I speculate this discrepancy relates to the expectation in the model that the aerosol is the same size as the beads and is forced to interact with them. In contrast, the experimental work relied on smaller aerosols relative to the beads providing a chance for aerosol to pass through the bed, potentially not contacting any polymer absorbent materials. In addition to finding the ability to block the xylene fog, I showed that the addition of the polymer bed on the nylon mesh support minimally impacted the breathability of the fabric. This result highlighted that a barrier material could be made to be highly breathable while remaining chemically protective.

5.2 Synthesis of Works

These individual works build on each other, and when combined, provide insight on further work and how it can be approached. While Chapter 3 discusses the development of a bulk scale polymer, in Chapter 4 I use the polymer in a powdered form. This could loopback into Chapter 3 by redeveloping the polymer in emulsion polymerizations in order to directly create beads. While this was initially tried with some success, the size distribution of the particles remained near 1 μm. This became an issue because the fabrics I investigated decreased from 34% to just 5% open area on decreasing the average polymer particle size from 40 μm to 5 μm. This reduction would have impacted breathability and reduced the potential usability of this system.

Connecting Chapter 2 with Chapter 4 provides an interesting insight that, while the microfractures do augment the dehydration rate, it is the stomata that lose the majority of water vapor. This suggests that composite fabrics could be further improved by utilizing areas with higher breathability for regions of high heat exchange (e.g. the

underarm). These regions would have a more open collapsible structure to provide high rates of breathability while retaining aerosol protection. In contrast, areas with low breathability requirements could use more dense fibers and restrict breathability but use a lower loading of absorbent polymer to retain protection. Coupling the changes in size for different areas of the body could provide high levels of protection with the minimal addition of the super absorbent polymer.

5.2 Future works

Further development is beyond the scope of this thesis; however this work provides a jumping point to explore many new ideas. In polymer development, there is a body of evidence that acrylamide chemistry is a very strong candidate on which to serve as a swelling platform.[38,40,110–114,44,50,53,79,91,107–109] Further investigation of this approach could provide a more fundamental analysis of how different chemical moieties attached to the acrylamide backbone augment swelling, especially by controlling solvent-polymer interactions to target specific molecules. Acrylamide gels have been shown to swell in diverse solvents such as oil,[53,101,113] alcohol,[114] and water.[48,94,115] By developing these polymers further, it could broaden our understanding and find novel functional uses for them. Additionally, gelled materials have unique properties that can be exploited to create shape change, allowing them to be used in a variety of applications.

In regard to further development of the composite fabric introduced in Chapter 4, one major hurdle that needs to be addressed is the breakdown/decontamination of the suit from CWAs and other hazardous chemicals. While I am able to capture and block most mass transport, retaining highly toxic materials near the skin is a very dangerous

45

proposition. One potential area that can be explored is using a Pickering emulsion to decorate the polymer beads with a decontaminating agent. By using nano-sized decontamination agent particles, the emulsion polymerization can be stabilized and the catalyst can be embedded to the surface creating a reactive swelling surface. This would provide the immediate protection required while also destroying the CWA to limit further risk of exposure to the wearer.

Finally, the other major limitation of the composite fabric concept is the attachment of polymer bed to the underlying fabric. I did not investigate adding an adhesive to anchor the polymer to the fabric. While compartmentalized pockets of unbound particles could work, a more reasonable expectation is to adhere the particles to the fibrous backbone to maintain uniform protection. Pressure sensitive adhesives, direct polymer anchoring, and fiber-polymer bonding should all be explored to determine the best way to prevent the absorbent moving or abrading from the surface. This work would extend the preliminary results to make a super absorbent polymer augmented fabric a viable protective system.

Models of this system, as done by Dr. Akshay Phadnis,[106] can provide key insights that combine with the experimental work and can continue to be used to inform the research process. While some of the conclusions derived from his work are applied to this work, there is still significant optimization that can be done to improve the performance of the protective fabric. Throughout this thesis I worked towards a breathable, wearable fabric that also provides chemical protection via stimuli-responsive polymers. While this work has created new insights and developments towards this goal, there is substantial further developed needed to achieve a commercializable product.

REFERENCES

1.   Kotagama, P., Phadnis, A., Manning, K. C. & Rykaczewski, K. Rational Design of
        Soft , Thermally Conductive Composite Liquid-Cooled Tubes for Enhanced
        Personal , Robotics , and Wearable Electronics Cooling. *Adv. Mater. Technol.* **4**,
        1800690 (1–12) (2019).

2.   Fornasiero, F. Water vapor transport in carbon nanotube membranes and
        application in breathable and protective fabrics. *Curr. Opin. Chem. Eng.* **16**, 1–8
        (2017).

3.   Hudiono, Y. C. *et al.* A highly breathable organic/inorganic barrier material that
        blocks the passage of mustard agent simulants. *Ind. Eng. Chem. Res.* **51**, 7453–
        7456 (2012).

4.   Spitz Steinberg, R., Cruz, M., Mahfouz, N. G. A., Qiu, Y. & Hurt, R. H.
        Breathable Vapor Toxicant Barriers Based on Multilayer Graphene Oxide. *ACS
        Nano* **11**, 5670–5679 (2017).

5.   Peng, C., Iqbal, Z., Sirkar, K. K. & Peterson, G. W. Graphene Oxide-Based
        Membrane as a Protective Barrier against Toxic Vapors and Gases. *ACS Appl.
        Mater. Interfaces* **12**, 11094–11103 (2020).

6.   Giannakoudakis, D. A., Barczak, M., Pearsall, F., O'Brien, S. & Bandosz, T. J.
        Composite porous carbon textile with deposited barium titanate nanospheres as
        wearable protection medium against toxic vapors. *Chem. Eng. J.* **384**, 123280
        (2020).

7.   Gorzkowska-Sobas, A. A. *Chemical Warfare Agents and Their Interactions with
        Solid Surfaces*; Rapport 00574; Norwegian Defense Research Establishment:
        Kjeller, Norway, 2013.

8.   Varady, M. J., Pearl, T. P., Stevenson, S. M. & Mantooth, B. A. Decontamination
        of VX from Silicone: Characterization of Multicomponent Diffusion Effects. *Ind.
        Eng. Chem. Res.* **55**, 3139–3149 (2016).

9.   Chambers, A. B. & Blackaby, J. R. A liquid cooled garment temperature controller
        based on sweat rate. (1972).

10.   Cadarette, B. S. *et al.* Intermittent microclimate cooling during exercise-heat stress
        in US army chemical protective clothing. *Ergonomics* **49**, 209–219 (2006).

11.   Dionne, J. P., Semeniuk, K., Makris, A., Teal, W. & Laprise, B. *Thermal manikin
        evaluation of liquid cooling garments intended for use in hazardous waste
        management*. (2003).

12. Kim, J.-H., Coca, A., Williams, W. J. & Roberge, R. J. Effects of liquid cooling garments on recovery and performance time in individuals performing strenuous work wearing a firefighter ensemble. *J. Occup. Environ. Hyg.* **8**, 409–416 (2011).

13. Gao, T. *et al.* Three-Dimensional Printed Thermal Regulation Textiles. *ACS Nano* **11**, 11513–11520 (2017).

14. Chen, X., Su, Y., Reay, D. & Riffat, S. Recent research developments in polymer heat exchangers - A review. *Renewable and Sustainable Energy Reviews* vol. 60 1367–1386 (2016).

15. Cao, H., Branson, D. H., Nam, J., Peksoz, S. & Farr, C. A. Development of a cooling capability test method for liquid-cooled textile system. *J. ASTM Int.* **2**, 1–10 (2005).

16. Webb, R. C. *et al.* Ultrathin conformal devices for precise and continuous thermal characterization of human skin. *Nat. Mater.* **12**, 938 (2013).

17. Terrier, D., Clayton, R., Whitlock, D. & Conger, B. *High Performance Mars Liquid Cooling and Ventilation Garment Project.* (2015) doi:JSC-CN-33642.

18. Kuznetz, L. H. Automatic control of human thermal comfort by a liquid-cooled garment. *J. Biomech. Eng.* **102**, 155–161 (1980).

19. Yang, Y., Stapleton, J., Diagne, B. T., Kenny, G. P. & Lan, C. Q. Man-portable personal cooling garment based on vacuum desiccant cooling. *Appl. Therm. Eng.* **47**, 18–24 (2012).

20. Hunter, I., Hopkins, J. T. & Casa, D. J. Warming up with an ice vest: Core body temperature before and after cross-country racing. *J. Athl. Train.* **41**, 371–374 (2006).

21. Almqvist, H., *Cooling Garment Having Phase Change Material In Its Extremity Portions.* US8499367B2. (2005).

22. Force, U. S. A. AFVA 10-2512: Mission Oriented Protective Postures. (2012).

23. Gonzalez, R. R., McLellan, T. M., Withey, W. R., Chang, S. K. & Pandolf, K. B. Heat strain models applicable for protective clothing systems: comparison of core temperature response. *J. Appl. Physiol.* **83**, 1017–1032 (1997).

24. Wartell, M., Kleinman, M. & Huey, B. *Strategies to protect the health of deployed US forces: force protection and decontamination. Health (San Francisco)* (1999).

25.   Wissler, E. H. *Human Temperature Control: A quantitative Approach*. (Springer, 2018).

26.   Nations, L. of. Protocol: For the Prohibition of the Use in War of Asphyxiating, Poisonous or Other Gases, and of Bacteriological Methods of Warfare. *UN Conventions* vol. 25 (1925).

27.   UN. *Convention on the Prohibition of the Development, Production, Stockpiling and Use of Chemical Weapons and on theirDestruction.* (1993).

28.   Bhaganagar, K. & Bhimireddy, S. R. Assessment of the plume dispersion due to chemical attack on April 4, 2017, in Syria. *Nat. Hazards* **88**, 1893–1901 (2017).

29.   Dolgin, E. Syrian gas attack reinforces need for better anti-sarin drugs. *Nat. Med.* **19**, 1194–1195 (2013).

30.   Sezigen, S. *et al.* Victims of chemical terrorism, a family of four who were exposed to sulfur mustard. *Toxicol. Lett.* **303**, 9–15 (2019).

31.   Johnson, N. H., Larsen, J. C. & Meek, E. *Historical Perspective of Chemical Warfare Agents*. *Handbook of Toxicology of Chemical Warfare Agents: Second Edition* (INC, 2015). doi:10.1016/B978-0-12-800159-2.00002-6.

32.   Bui, N. *et al.* Ultrabreathable and Protective Membranes with Sub-5 nm Carbon Nanotube Pores. *Adv. Mater.* **28**, 5871–5877 (2016).

33.   Fornasiero, F. Water vapor transport in carbon nanotube membranes and application in breathable and protective fabrics. *Curr. Opin. Chem. Eng.* **16**, 1–8 (2017).

34.   Sha, S. C., Zhu, R., Herbert, M. B., Kalow, J. A. & Swager, T. M. Chemical warfare simulant-responsive polymer nanocomposites: Synthesis and evaluation. *J. Polym. Sci. Part A Polym. Chem.* **55**, 3034–3040 (2017).

35.   Liu, X., Li, Y., Hu, J., Jiao, J. & Li, J. Smart moisture management and thermoregulation properties of stimuli-responsive cotton modified with polymer brushes. *RSC Adv.* **4**, 63691–63695 (2014).

36.   Mashkoor, F., Nasar, A. & Inamuddin. Carbon nanotube-based adsorbents for the removal of dyes from waters: A review. *Environ. Chem. Lett.* **18**, 605–629 (2020).

37.   Erdely, A. *et al.* Carbon nanotube dosimetry: From workplace exposure assessment to inhalation toxicology. *Part. Fibre Toxicol.* **10**, 1–14 (2013).

38. Hooper, H. H., Baker, J. P., Blanch, H. W. & Prausnitz, J. M. Swelling equilibria for positively ionized polyacrylamide hydrogels. *Macromolecules* **23**, 1096–1104 (1990).

39. Chang, C., Duan, B., Cai, J. & Zhang, L. Superabsorbent hydrogels based on cellulose for smart swelling and controllable delivery. *Eur. Polym. J.* **46**, 92–100 (2010).

40. Chen, J., Park, H. & Park, K. Synthesis of superporous hydrogels: Hydrogels with fast swelling and superabsorbent properties. *J. Biomed. Mater. Res.* **44**, 53–62 (1999).

41. Chauhan, K., Chauhan, G. S. & Ahn, J. H. Synthesis and characterization of novel guar gum hydrogels and their use as Cu2+ sorbents. *Bioresour. Technol.* **100**, 3599–3603 (2009).

42. Peralta Ramos, M. L. *et al.* Chitin hydrogel reinforced with TiO2 nanoparticles as an arsenic sorbent. *Chem. Eng. J.* **285**, 581–587 (2016).

43. Panic, V. V., Madzarevic, Z. P., Volkov-Husovic, T. & Velickovic, S. J. Poly(methacrylic acid) based hydrogels as sorbents for removal of cationic dye basic yellow 28: Kinetics, equilibrium study and image analysis. *Chem. Eng. J.* **217**, 192–204 (2013).

44. Wang, Q., Wilfong, W. C., Kail, B. W., Yu, Y. & Gray, M. L. Novel Polyethylenimine-Acrylamide/SiO2 Hybrid Hydrogel Sorbent for Rare-Earth-Element Recycling from Aqueous Sources. *ACS Sustain. Chem. Eng.* **5**, 10947–10958 (2017).

45. Zhou, G. *et al.* A highly efficient polyampholyte hydrogel sorbent based fixed-bed process for heavy metal removal in actual industrial effluent. *Water Res.* **89**, 151–160 (2016).

46. Brandl, F. *et al.* Hydrogel-based drug delivery systems: Comparison of drug diffusivity and release kinetics. *J. Control. Release* **142**, 221–228 (2010).

47. Ashley, G. W., Henise, J., Reid, R. & Santi, D. V. Hydrogel drug delivery system with predictable and tunable drug release and degradation rates. *Proc. Natl. Acad. Sci. U. S. A.* **110**, 2318–2323 (2013).

48. Peppas, N. A. Hydrogels and drug delivery. *Curr. Opin. Colloid Interface Sci.* **2**, 531–537 (1997).

49. Fumasi, F. M., Stephanopoulos, N. & Holloway, J. L. Reversible control of biomaterial properties for dynamically tuning cell behavior. *J. Appl. Polym. Sci.* **137**, 1–16 (2020).

50. Tse, J. R. & Engler, A. J. Preparation of hydrogel substrates with tunable mechanical properties. *Curr. Protoc. Cell Biol.* 1–16 (2010) doi:10.1002/0471143030.cb1016s47.

51. Kuo, C. K. & Ma, P. X. Ionically crosslinked alginate hydrogels as scaffolds for tissue engineering: Part 1. Structure, gelation rate and mechanical properties. *Biomaterials* **22**, 511–521 (2001).

52. Ono, T., Sugimoto, T., Shinkai, S. & Sada, K. Lipophilic polyelectrolyte gels as super-absorbent polymers for nonpolar organic solvents. *Nat. Mater.* **6**, 429–433 (2007).

53. Ono, T., Sugimoto, T., Shinkai, S. & Sada, K. Molecular design of superabsorbent polymers for organic solvents by crosslinked lipophilic polyelectrolytes. *Adv. Funct. Mater.* **18**, 3936–3940 (2008).

54. Kukkonen, J., Riikonen, K., Nikmo, J., Jäppinen, A. & Nieminen, K. Modelling aerosol processes related to the atmospheric dispersion of sarin. **85**, 165–179 (2001).

55. Zhong, Y. *et al.* Reversible Humidity Sensitive Clothing for Personal Thermoregulation. *Sci. Rep.* **7**, 44208 (2017).

56. Makino, K., Mack, E. J., Okano, T. & Sung Wan Kim. A microcapsule self-regulating delivery system for insulin. *J. Control. Release* **12**, 235–239 (1990).

57. Siegel, R. A. & Firestone, B. A. Mechanochemical approaches to self-regulating insulin pump design. *J. Control. Release* **11**, 181–192 (1990).

58. He, X. *et al.* Synthetic homeostatic materials with chemo-mechano-chemical self-regulation. *Nature* **487**, 214–218 (2012).

59. Moghaddam, S., Pengwang, E., Masel, R. I. & Shannon, M. A. A self-regulating hydrogen generator for micro fuel cells. *J. Power Sources* **185**, 445–450 (2008).

60. Park, C. H. *et al.* Nanocrack-regulated self-humidifying membranes. *Nature* **532**, 480–483 (2016).

61. Nisbet, R. A. & Patten, D. T. Seasonal temperature acclimation of a prickly-pear cactus in south-central Arizona. *Oecologia* **15**, 345–352 (1974).

62. Altman, P. & Dittmer, D. *Environmental Biology*. (Federation of American Societies for Experimental Biology, 1966).

63. Anderson, E. F. *The cactus family*. (Portland, Or. : Timber Press, 2001).

64. Mallona, I., Egea-Cortines, M. & Weiss, J. Conserved and divergent rhythms of Crassulacean acid metabolism-related and core clock gene expression in the cactus Opuntia ficus-indica. *Plant Physiol.* **156**, 1978–1989 (2011).

65. Edwards, E. J. & Donoghue, M. J. and the Origin of the Cactus Life-Form. *Am. Nat.* **167**, 777–793 (2006).

66. Acevedo, E., Badilla, I. & Nobel, P. S. Water Relations, Diurnal Acidity Changes, and Productivity of a Cultivated Cactus, Opuntia ficus-indica. *Plant Physiol.* **72**, 775–780 (1983).

67. Clark, D. Images of Leaf Stomata: Little Things that Matter. *Micros. Today* **27**, 12–17 (2019).

68. Ben Salem-Fnayou, A., Zemni, H., Nefzaoui, A. & Ghorbel, A. Micromorphology of cactus-pear (opuntia ficus-indica (L.) mill) cladodes based on scanning microscopies. *Micron* **56**, 68–72 (2014).

69. Rykaczewski, K. *et al.* Microscale Mechanism of Age Dependent Wetting Properties of Prickly Pear Cacti (Opuntia). *Langmuir* **32**, 9335–9341 (2016).

70. Barcikowski, W. & Nobel, P. S. Water Relations of Cacti During Desiccation: Distribution of Water in Tissues. *Bot. Gaz.* **145**, 110–115 (1984).

71. Cassie, A. B. D. & Baxter, S. Wettability of porous surfaces. *Trans. Faraday Soc.* **40**, 546 (1944).

72. Smith, M., Hargroves, K., Smith, M. & Hargroves, K. Innovation inspired by nature: Biomimicry. *ECOS* **2006**, 27–29 (2006).

73. Akber Hassan, W. A. & Jiang, X. Upscaling and its application in numerical simulation of long-term CO2 storage. *Greenh. Gases Sci. Technol.* **2**, 408–418 (2012).

74. Park, Y. I. & Lee, K. H. Preparation of water-swollen hydrogel membranes for gas separation. *J. Appl. Polym. Sci.* **80**, 1785–1791 (2001).

75. Mittenthal, M. S. *et al.* Ionic Polyimides: Hybrid Polymer Architectures and Composites with Ionic Liquids for Advanced Gas Separation Membranes. *Ind. Eng. Chem. Res.* **56**, 5055–5069 (2017).

76. Mohshim, D. F., Mukhtar, H. & Man, Z. Composite blending of ionic liquid–poly(ether sulfone) polymeric membranes: Green materials with potential for carbon dioxide/methane separation. *J. Appl. Polym. Sci.* **133**, 1–8 (2016).

77. Ward, W. J. & Robb, W. L. Carbon Dioxide-Oxygen Separation : Facilitated Transport of Carbon Dioxide across a Liquid Film. *Am. Assoc. Adv. Sci.* **156**, 1481–1484 (1967).

78. Fan, J. B. *et al.* Directly Coating Hydrogel on Filter Paper for Effective Oil-Water Separation in Highly Acidic, Alkaline, and Salty Environment. *Adv. Funct. Mater.* **25**, 5368–5375 (2015).

79. Hosseinzadeh, H. & Mohammadi, S. Synthesis of a Novel Hydrogel Nanocomposite Coated on Cotton Fabric for Water-Oil Separation. *Water, Air, Soil Pollut.* **225**, (2014).

80. Kota, A. K., Kwon, G., Choi, W., Mabry, J. M. & Tuteja, A. Hygro-responsive membranes for effective oil–water separation. *Nat. Commun.* **3**, 1025 (2012).

81. Ju, H. *et al.* Crosslinked poly(ethylene oxide) fouling resistant coating materials for oil/water separation. *J. Memb. Sci.* **307**, 260–267 (2008).

82. Liu, N. *et al.* A facile solvent-manipulated mesh for reversible oil/water separation. *ACS Appl. Mater. Interfaces* **6**, 12821–12826 (2014).

83. Zhang, L., Zhong, Y., Cha, D. & Wang, P. A self-cleaning underwater superoleophobic mesh for oil-water separation. *Sci. Rep.* **3**, 2326 (2013).

84. Zhu, H., Qiu, S., Jiang, W., Wu, D. & Zhang, C. Evaluation of electrospun polyvinyl chloride/polystyrene fibers as sorbent materials for oil spill cleanup. *Environ. Sci. Technol.* **45**, 4527–4531 (2011).

85. Holland, H. W. Bilge Oil Absorber and Solidifier. US005458773A. (1994).

86. Deschamps, G., Caruel, H., Borredon, M. E., Bonnin, C. & Vignoles, C. Oil removal from water by selective sorption on hydrophobic cotton fibers. 1. Study of sorption properties and comparison with other cotton fiber-based sorbents. *Environ. Sci. Technol.* **37**, 1013–1015 (2003).

87. Hayase, G., Kanamori, K., Fukuchi, M., Kaji, H. & Nakanishi, K. Facile synthesis of marshmallow-like macroporous gels usable under harsh conditions for the separation of oil and water. *Angew. Chemie - Int. Ed.* **52**, 1986–1989 (2013).

88. Li, X. *et al.* Direct Oil Recovery from Saturated Carbon Nanotube Sponges. *ACS Appl. Mater. Interfaces* **8**, 12337–12343 (2016).

89. Gupta, S. & Tai, N.-H. Carbon materials as oil sorbents: a review on the synthesis and performance. *J. Mater. Chem. A* **4**, 1550–1565 (2016).

90. Ma, M. & Hill, R. M. Superhydrophobic surfaces. *Curr. Opin. Colloid Interface Sci.* **11**, 193–202 (2006).

91. Ohmine, I. Salt effects on the phase transition of ionic gels. *J. Chem. Phys.* **77**, 5725 (1982).

92. Boddu, V. M. *et al. Lipophilic Super-Absorbent Swelling Gels as Cleaners for Use on Weapons Systems and Platforms Final Report*. (2011).

93. Mamada, A., Tanaka, T., Kungwatchakun, D. & Irie, M. Photoinduced Phase Transition of Gels. *Macromolecules* **23**, 1517–1519 (1990).

94. Zhang, X., Li, Y., Hu, Z. & Littler, C. L. Bending of N-isopropylacrylamide gel under the influence of infrared light. *J. Chem. Phys.* **102**, 551–555 (1995).

95. Flory, P. J. *Principles of polymer chemistry*. (Cornell University Press, 1953). doi:10.1002/pen.760050321.

96. Patterson, D. & Delmas, G. New Aspects of Polymer Solution Thermodynamics. *Off. Dig. Fed. Soc. Paint Technol.* **34**, 677–692, (1962).

97. Hansen, C. M. *Hansen Solubility Parameters: A User's Handbook*. (CRC Press, 2000).

98. Peplow, M. A century of chemical warfare: nations reflect on grim anniversary. *Nature* (2015) doi:10.1038/nature.2015.17381.

99. Yang, Y., Rana, D., Lan, C. Q. & Matsuura, T. Development of Membrane-based Desiccant Fiber for Vacuum Desiccant Cooling. *ACS Appl. Mater. Interfaces* (2016).

100. Kotagama, P., Phadnis, A., Manning, K. C. & Rykaczewski, K. Rational Design of Soft, Thermally Conductive Composite Liquid-Cooled Tubes for Enhanced Personal, Robotics, and Wearable Electronics Cooling. *Adv. Mater. Technol.* **1800690**, 1–12 (2019).

101. Manning, K. C., Phadnis, A., Simonet, D., Burgin, T. P. & Rykaczewski, K. Development of a Nonelectrolytic Selectively Superabsorbent Polymer. *Ind. Eng. Chem. Res.* **57**, 13269–13274 (2018).

102. Donnelly, T. D., Hogan, J., Mugler, A., Schubmehl, M. & Schommer, N. Using ultrasonic atomization to produce an aerosol of micron-scale particles. 1–10 (2005) doi:10.1063/1.2130336.

103. J. Allen Zak. *Drop Size Distributions and Related Properties of Fog for Five Locations Measured From Aircraft*. (1994) doi:10.1175/1520-0477(1998)079.

104. ASTM. Standard Test Methods for Water Vapor Transmission of Materials E96/E96M. *Annu. B. ASTM Stand.* **i**, 1–10 (2016).

105. Phadnis, A., Manning, K. C., Sanders, I., Burgin, T. P. & Rykaczewski, K. Droplet-train induced spatiotemporal swelling regimes in elastomers. *Soft Matter* **14**, 5869–5877 (2018).

106. Phadnis, A. Using Droplet Induced Deformations in Polymeric Functional Materials for Heat and Mass Transport Modulation. *Arizona State University*.

107. Uz Okay, O. & Sariisik, S. B. Swelling behavior of poly(acrylamide-co-sodium acrylate) hydrogels in aqueous salt solutions: theory versus experiments. *Eur. Polym. J.* **36**, 393–399 (2000).

108. Sotoudeh, S. *et al.* Dynamical Modeling and Experimental Analysis on the Swelling Behavior of the sIPN Hydrogels. *Ind. Eng. Chem. Res.* **49**, 10111–10115 (2010).

109. Achilleos, E. C., Prud'homme, R. K., Kevrekidis, I. G., Christodoulou, K. N. & Gee, K. R. Quantifying deformation in gel swelling: Experiments and simulations. *Aiche J.* **46**, 2128–2139 (2000).

110. Luo, L., Kato, M., Tsuruta, T., Kataoka, K. & Nagasaki, Y. Stimuli-sensitive polymer gels that stiffen upon swelling. *Macromolecules* **33**, 4992–4994 (2000).

111. Zhang, X., Li, Y., Hu, Z. & Littler, C. L. Bending of N-isopropylacrylamide gel under the influence of infrared light. *J. Chem. Phys.* **102**, 551–555 (1995).

112. Zarzar, L. D. & Aizenberg, J. Stimuli-responsive chemomechanical actuation: A hybrid materials approach. *Acc. Chem. Res.* **47**, 530–539 (2014).

113. Ono, T. & Sada, K. Toward the design of superabsorbent materials for non-polar organic solvents and oils: ionic content dependent swelling behaviour of cross-linked poly(octadecyl acrylate)-based lipophilic polyelectrolytes. *J. Mater. Chem.* **22**, 20962 (2012).

114. Ozmen, M. M. & Okay, O. Swelling behavior of strong polyelectrolyte poly(N - t - butylacrylamide-co-acrylamide) hydrogels. *Eur. Polym. J.* **39**, 877–886 (2003).

115. Wandera, D., Wickramasinghe, S. R. & Husson, S. M. Stimuli-responsive membranes. *J. Memb. Sci.* **357**, 6–35 (2010).

116. Binev, Y., Marques, M. M. B. & Aires-de-Sousa, J. Prediction of1H NMR coupling constants with associative neural networks trained for chemical shifts. *J. Chem. Inf. Model.* **47**, 2089–2097 (2007).

117. Castillo, A. M., Patiny, L. & Wist, J. Fast and accurate algorithm for the simulation of NMR spectra of large spin systems. *J. Magn. Reson.* **209**, 123–130 (2011).

APPENDIX A

SUPPORTING CODES FOR LINE PROFILES IN CHAPTER 2

These codes, unless otherwise stated, were all custom developed to analyze the

crack profiles. Code sections are separated by a line break with all non-stock MATLAB

code listed in this appendix.

Cactus Surface Analyzer Main Code:

```
---------------------------------------------------------
%Read Optical profilometer file and extract the relevant map of heights
ReadZMP_ES

%Extract the cracks from the image of the cactus surface
[crack_data2] = crack_definer (Map);

%Write the line profiles to a variable to be viewed and analyzed for depth, width, and
%shape
[profiles2] = crack_profiles (crack_data,Map);
---------------------------------------------------------
```

ReadZMP_ES Function, written by Wolfgang Kaehler for Zygo Inc. Provided for this
analysis for free, please see the copyright holder (Zygo) for a copy of the code.

```
----------------------------------------------------------------
function [crack_data] = crack_definer (Map)
%crack_definer takes the 2D projection of the cactus surface and allows the
%user to manually specify a crack by data points along the crack line.
%This information is then sorted to create a set of points that are aligned
%to their nearest neighbors on the image

%Outputs x,y data in a single array of paired values


    %View the 2D projection of the surface
    imagesc(Map)
    colormap('hot')
    hold on
    %Toggle - 'Yes' 'No' or 'Cancel'
    toggle = 'Cancel';

    %Get the first crack
    while length(toggle) == 6
    [a,b] = getpts;
    [a , b] = crk_org (a,b);
    a(end+1) = -1;
    b(end+1) = -1;
    toggle = questdlg('Additional cracks to classify?');
    end

    %Add previous crack points to the image
    while length(toggle)>2
       plot(a,b,'o','MarkerEdgeColor','k')
      [c,d] = getpts;
      [c,d] = crk_org (c,d);
      toggle = questdlg('Additional cracks to classify?');
      if length(toggle)<4
         a(end+1:end+length(c)) = c;
         b(end+1:end+length(d)) = d;
         a(end+1) = -1;
         b(end+1) = -1;
      end
    end
    crack_data = [a,b];

end
----------------------------------------------------------------
```

```
----------------------------------------------------------------
function [profile] = line_extract_1(xs,ys,tol,im)
%Uses 2 points inside a crack to define the profile of the first point
%[x(1),y(1)]
%tol is the minimum number of pixels to move perpendicularly
%im is the image map from ZMP file

%xs and ys must be integers because we are pulling points from the grid
xs = round(xs);
ys = round(ys);

%Debug toggle
debug = 1;

B = reshape(ys,2,1); %avoids error from vertical vs horizontal vector
A = [1,xs(1);1,xs(2)]; %Matrix for linear algebra solving
lin_coeffs = A\B; %Coefficients from linear solving
m = -1/lin_coeffs(2); %Slope perpendicular to the two points

x_pix = tol;
y_pix = round(abs(m)*tol);


if x_pix < y_pix

    y_pix = tol;
    x_pix = round(abs(1/m)*tol);
    %swap x and y values to make horizontal not vertical - just to reuse code
    x=[ys(1)+y_pix ys(1)-y_pix];
    y=[xs(1)+x_pix xs(1)-x_pix];

    %set any out of bounds points to the minimum 1
    x(x<=0)=1;
    y(y<=0)=1;
    %%%%RESET POINTS FOR VALUES GOING TO 1%%%%

    %reshuffle so we go from small x to large x
    if x(2)<x(1)
        x = flip(x);
        if sign((y(2)-y(1))/(x(2)-x(1)))~=sign(m)
            y = flip(y);
        end
    end

        X=x(1):x(2);
```

```matlab
        Y=round(interp1(x,y,X));
        profile = im(round(mean(Y)),X);


    %For Debugging
    if debug==1
        imagesc(im)
        hold on
        plot(Y,X,'r',xs,ys,'o')
        pause
        % close gcf
    end

else
    x=[xs(1)+x_pix xs(1)-x_pix];
    y=[ys(1)+y_pix ys(1)-y_pix];

    %set any out of bounds points (Outside the image map) to the minimum 1
    x(x<=0)=1;
    y(y<=0)=1;
    %%%%RESET POINTS FOR VALUES GOING TO 1%%%%

    %reshuffle so we go from small x to large x
    if x(2)<x(1)
        x = flip(x);
        if sign((y(2)-y(1))/(x(2)-x(1)))~=sign(m)
            y = flip(y);
        end
    end

    X=x(1):x(2);
    Y=round(interp1(x,y,X));
    profile = im(round(mean(Y)),X);

    %For Debugging
    if debug == 1
        imagesc(im)
        hold on
        plot(X,Y,'b',xs,ys,'o')
        pause
        % close gcf
    end
end
```

```matlab
--------------------------------------------------------------
function [profiles] = crack_profiles (crack_data,im)

%Tolerance for profile % of resolution to extend in either direction
tol =round(0.04*max(size(im)));

%preallocate profiles variable
profiles = zeros(2*tol+1,length(crack_data));

%define crack stop/start points
breaks = find(crack_data(:,1)==-1);
breaks = [0;breaks];

for i = 2:length(breaks)
    crack = crack_data(breaks(i-1)+1:breaks(i)-1,:);

    for j = 1:length(crack)-1
        profiles(:,j+breaks(i-1)) = line_extract_1(crack(j:j+1,1),crack(j:j+1,2),tol,im);
    end
end
end
--------------------------------------------------------------
```

APPENDIX B

SUPPORTING INFORMATION FOR CHAPTER 3

B1 NMR results and analysis

To determine sample purity, the NMR spectra were compared against theoretical equivalents that were generated using the nmrdb software, which is a validated prediction tool for NMR spectra.[116,117] All experimental peaks were characterized and identified as shown in Figure S1(a). Using the spectrum, the remaining starting amine was identified by the characteristic resonance at ~3.1 ppm. This peak, shown in Figure B1(b), represents the 2 hydrogens next to the nitrogen in the amine. By dividing the integrated peak value in Figure B1(b) (0.0019) by the value obtained for a peak unique to the desired product representing the same number of hydrogens, the percent of the remaining amine was estimated to be below 0.1%, with some samples having no detectable levels of the starting amine.
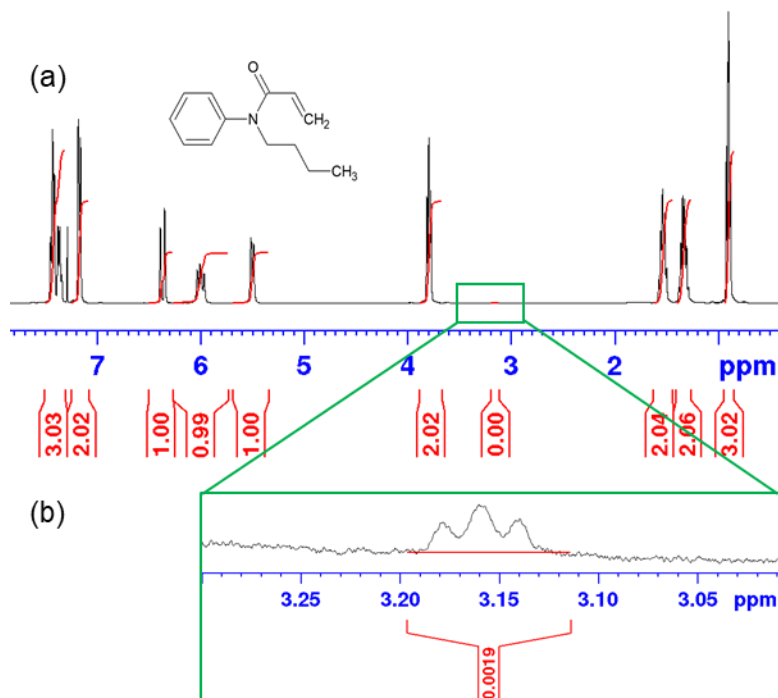

Figure B1. Representative NMR spectrum of the synthesized N,N-butylphenylacrylamide monomer: (a) the entire tested range showing peak integration in red and (b) close up of the characteristic precursor resonance used for monomer purity characterization.

B2 Miscible Solvent Swelling

Using tetrahydrofuran (THF) and water, representative blends of high and low swelling solvents were tested for polymer swelling. The mixtures were made by adding known volumes of THF and water to vials and vigorously mixing the blends before adding polymer to the mixture.
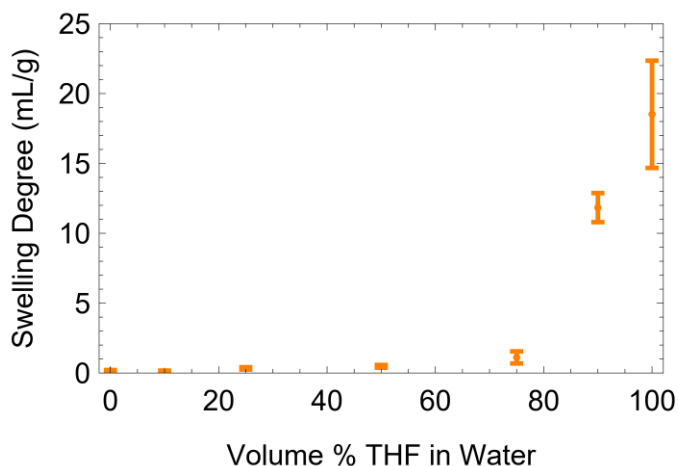

Figure B2. Swelling of the polymer in THF-water blends after 24-hour submersion.

B3 Swelling Kinetics in *o*-xylene

The polymer kinetics for swelling were tested on polymer prepared using the 1.25 mol% PEG 200 cross-linker. Polymer weights were recorded as the swelling occurred by removing the chip from the solvent bath and weighing it on an analytical balance. The chip was quickly replaced in the bath and the time resumed to determine the shape of the kinetic swelling behavior. I chose *o*-xylene as the solvent for this study due to its low vapor pressure, which limits artefacts stemming from the solvent evaporation during the frequent weight measurements.
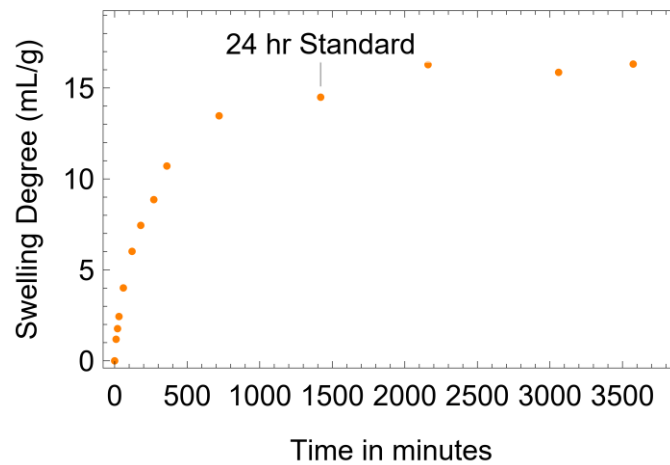
Figure B3. Kinetic swelling data of a representative polymer sample in *o*-xylene. Standard swelling measurement time noted at 24 hours.

APPENDIX C

PARTICLE SIZE DISTRIBUTION AND MEASUREMENTS FOR CHAPTER 4

C1 SAP particle size distribution

Using optical microscopy, I estimated the effective diameter of the SAP particles. While the particles show non-spherical geometry (typical for ground materials) I used the cross-sectional area, measured using ImageJ, to estimate the effective diameter for the equivalent area sphere. These diameters were then averaged by number to provide an estimate of the average particle size (44 ± 19 μm).
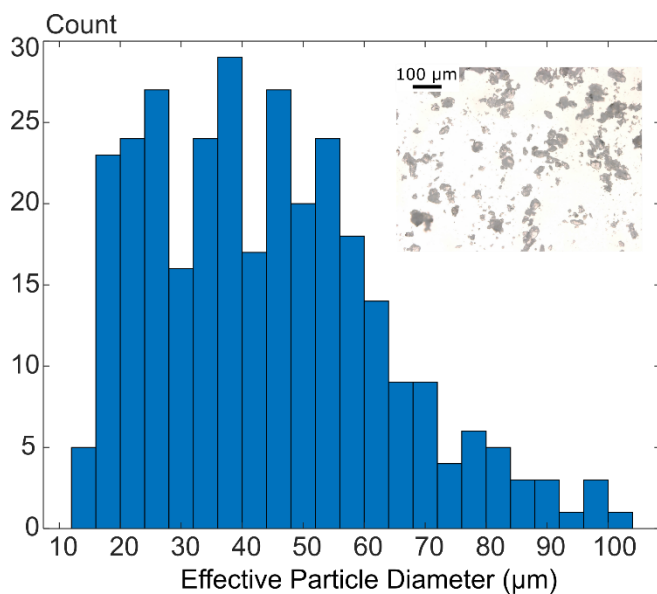

Figure C1. The effective diameters of the super absorbent polymer particles. Inset shows a representative image taken from the optical microscope.

C2 SAP swelling rates

We tested polymer swelling on the bead of SAP depositing a 2 μL droplet of *o*-xylene on a very thinly coated mesh. The results were captured using a Zeiss AxioVision microscope as a time lapse.
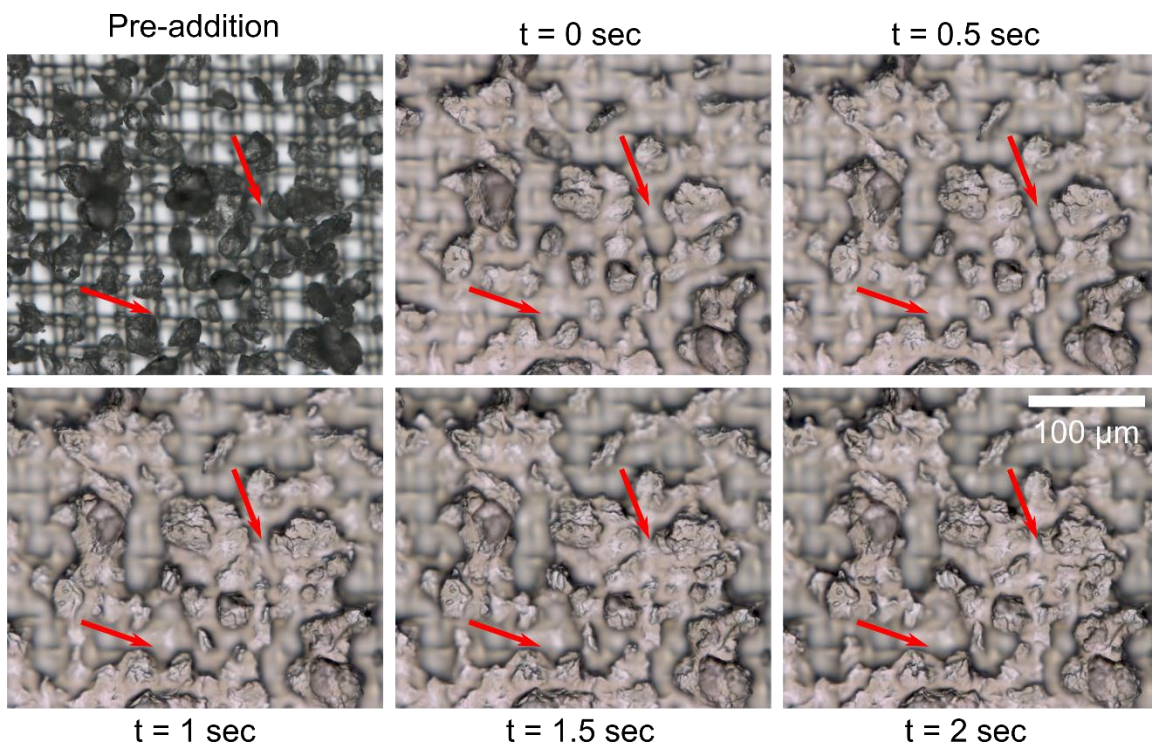
Figure C2. Time lapse of powdered polymer swelling in o-xylene dyed with oil red. The image in t = 0 seconds is split between the pre (left) and post (right) exposure at the same timepoint for comparative purposes.